ARTICLES
PUBLISHED ONLINE: 15 SEPTEMBER 2013 | DOI: 10.1038/NMAT3755
nature materials

# Ultrathin conformal devices for precise and continuous thermal characterization of human skin

R. Chad Webb[1†], Andrew P. Bonifas[1†], Alex Behnaz[2], Yihui Zhang[3,4], Ki Jun Yu[5], Huanyu Cheng[4], Mingxing Shi[6], Zuguang Bian[4,7], Zhuangjian Liu[8], Yun-Soung Kim[1], Woon-Hong Yeo[1], Jae Suk Park[5], Jizhou Song[9], Yuhang Li[4], Yonggang Huang[4], Alexander M. Gorbach[2] and John A. Rogers[1*]

**Precision thermometry of the skin can, together with other measurements, provide clinically relevant information about cardiovascular health, cognitive state, malignancy and many other important aspects of human physiology. Here, we introduce an ultrathin, compliant skin-like sensor/actuator technology that can pliably laminate onto the epidermis to provide continuous, accurate thermal characterizations that are unavailable with other methods. Examples include non-invasive spatial mapping of skin temperature with millikelvin precision, and simultaneous quantitative assessment of tissue thermal conductivity. Such devices can also be implemented in ways that reveal the time-dynamic influence of blood flow and perfusion on these properties. Experimental and theoretical studies establish the underlying principles of operation, and define engineering guidelines for device design. Evaluation of subtle variations in skin temperature associated with mental activity, physical stimulation and vasoconstriction/dilation along with accurate determination of skin hydration through measurements of thermal conductivity represent some important operational examples.**

Traditional methods for skin thermography use either sophisticated infrared digital cameras for spatial imaging or simple, paste-on temperature sensors for single-point measurements. These and other related technologies have value in certain contexts, but they do not offer continuous, cost-effective precision mapping capabilities that are required for use at the point of care. For example, infrared cameras provide millikelvin precision and fine resolution in imaging, but they are expensive and require immobilization of the patient. Point contact sensors avoid these limitations, but they do not have the ability to perform spatial mapping, as typically required to extract meaningful information across the structurally and functionally heterogeneous surface of the skin. Such devices also irritate the skin and modify its natural physiological responses by thermally and mechanically loading its surface.

Here we introduce a class of thermal characterization technology that combines precision measurement with mapping capabilities, in a form that integrates intimately and non-invasively onto the surface of the skin. The devices incorporate microscale temperature sensors that can simultaneously act as micro-heaters (actuators), in arrayed layouts on thin, low modulus elastic sheets. The sensors/actuators rely on either thin serpentine features of thin metal (50 nm thick; Au) or PIN diodes constructed with nanoscale membranes of silicon (320 nm thick; Si nanomembranes). Integrated collections of such components offer mechanical properties and geometries matched to human tissue[1], through advanced application of emerging concepts in stretchable electronics[2]. A key enabling characteristic for use on the skin is the ability to provide soft, conformal contact with the epidermis in a manner that does not constrain or alter natural motions or behaviours. This epidermal[2] design enables robust adhesion with minimal irritation or discomfort, and without measurement artefacts that can arise from relative motion of the sensors/actuators and the skin or from interference with processes such as transdermal water loss. Here, we describe these technologies and illustrate their capabilities in continuous thermal characterization of the epidermis. Examples range from temperature measurement with a precision that matches the most sophisticated infrared cameras, to assessment of thermal conductivity and effects of blood flow on thermal transport.

We built two types of system. The first consists of arrays of temperature sensors that rely on the temperature coefficient of resistance (TCR) in thin (50 nm), narrow (20 μm) serpentine traces of gold, fabricated using microlithographic techniques (Supplementary Note S1) and configured for direct external addressing. The second exploits multiplexed arrays of sensors based on PIN diodes formed by patterned doping of Si nanomembranes (Supplementary Note S2). Here, changes in temperature cause well-defined shifts in the turn-on voltage. In both cases, the

[1]Department of Materials Science and Engineering, University of Illinois at Urbana-Champaign, Urbana, Illinois 61801, USA, [2]National Institute of Biomedical Imaging and Bioengineering, National Institutes of Health, Bethesda, Maryland 20892, USA, [3]Center for Mechanics and Materials, Tsinghua University, Beijing 100084, China, [4]Department of Civil and Environmental Engineering, Department of Mechanical Engineering, Center for Engineering and Health, and Skin Disease Research Center, Northwestern University, Evanston, Illinois 60208, USA, [5]Department of Electrical and Computer Engineering, University of Illinois at Urbana-Champaign, Urbana, Illinois 61801, USA, [6]School of Mechanics and Engineering, Southwest Jiaotong University, Chengdu 610031, China, [7]Ningbo Institute of Technology, Zhejiang University, Ningbo 315100, China, [8]Institute of High Performance Computing, 1 Fusionopolis Way, #16-16 Connexis, Singapore 138632, Singapore, [9]Department of Mechanical and Aerospace Engineering, University of Miami, Coral Gables, Florida 33146, USA. [†]These authors contributed equally to this work. *e-mail: jrogers@illinois.edu

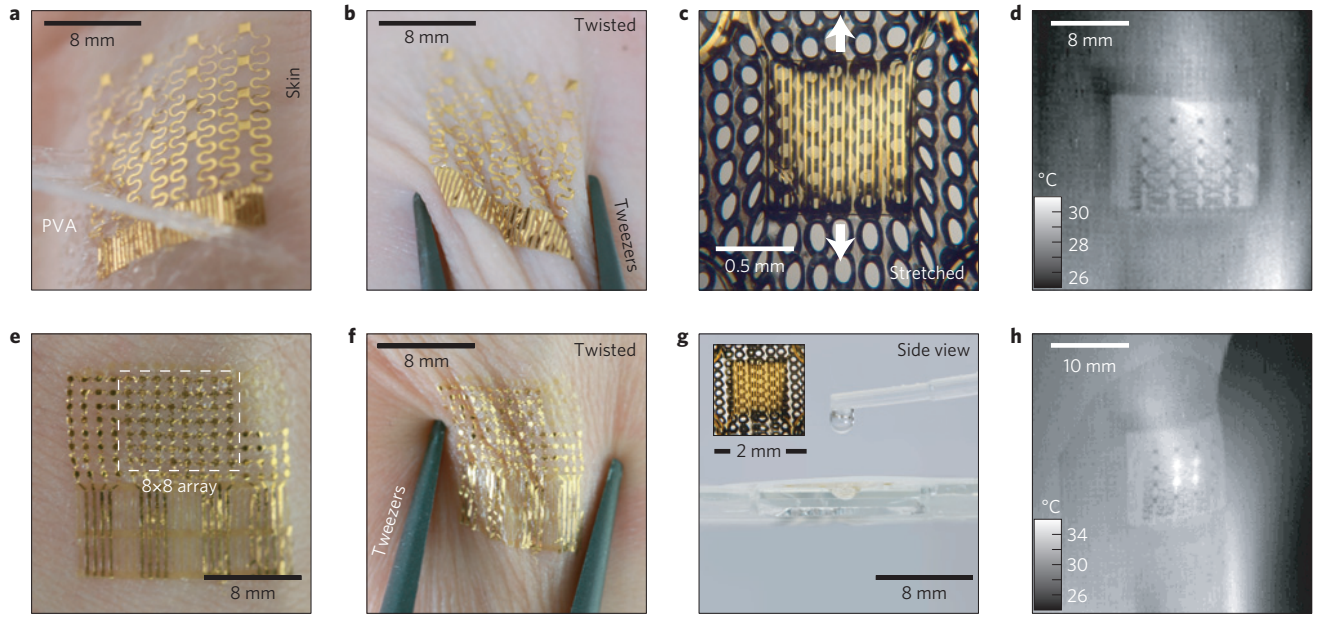


**Figure 1 | Ultrathin, compliant, skin-like arrays of precision temperature sensors and heaters. a**, Image of a 4 × 4 TCR sensor array after application to the skin using a water-soluble adhesive tape based on poly(vinyl alcohol). **b**, Similar device, deformed by pinching the skin in a twisting motion. **c**, Magnified image of a related device on a microperforated elastomeric substrate, under tensile strain. **d**, Infrared image of a 4 × 4 TCR sensor array mounted on the wrist at a location near the ulnar artery. **e**, Image of a 8 × 8 Si nanomembrane diode sensor array mounted on the skin. **f**, Similar device as deformed by pinching the skin in a twisting motion. **g**, Image of a 4 × 4 TCR sensor array mounted on microperforated elastomeric substrate, showing the ability of water to pass through readily. Inset: magnified image of a single TCR sensor on a microperforated substrate. **h**, Infrared image of a 4 × 4 TCR array on the human wrist while heating the four inner-most elements.

devices can be used as temperature sensors, as local microscale heaters, or as both, simultaneously. Figure 1 shows representative systems supported by thin (50 μm) uniform or microperforated elastomeric substrates, or integrated directly onto the human skin. The TCR device combines 16 sensors (each ∼1 mm × 1 mm, in a 4 × 4 layout) with interconnect traces (30 μm wide and 600 nm thick) in a filamentary serpentine mesh. Thin layers of polyimide (1.2 μm) encapsulate these structures from above and below, to provide electrical insulation and a moisture barrier (Fig. 2a). This construction also places the metal close to the neutral mechanical plane, for improved mechanical robustness. The filamentary mesh design minimizes strain in the sensors and interconnects during deformation. The PIN system (Fig. 2c) combines 64 sensors (each ∼100 μm × 200 μm, an 8 × 8 layout) in a similar mesh structure, but with an interconnect design that allows multiplexed addressing. The resulting layout reduces the number of external connections from 128 (direct addressing) to 16 (multiplexed addressing), and allows straightforward scaling to increased numbers of sensors. The devices mount directly onto the skin or onto thin, uniform or microperforated sheets of silicone elastomer (50 μm, 30 kPa). Conformal attachment to the skin in all cases occurs through the action of van der Waals forces alone. The effective moduli of the systems are comparable to or smaller than that of the epidermis thereby yielding a type of integration that is mechanically invisible to the user. Devices are typically applied to skin that is mostly hairless (glabrous) or shaved. Small amounts of hair can be accommodated, as shown in Supplementary Fig. S1. A thin, flexible, conductive cable (Elform, HST-9805-210) establishes connection to external control and data acquisition electronics. Typical measurements involve averaged outputs sampled at 2 or 0.5 Hz, to yield precision (one standard deviation) of ∼12 mK ($n = 222$) or ∼8 mK ($n = 55$), respectively, as evaluated in control experiments. Use on human skin in hospital settings increases noise slightly, resulting in a precision of ∼23 mK sampled at 2 Hz ($n = 300$) or ∼14 mK sampled at 0.5 Hz ($n = 75$; Supplementary Figs S2d,e and S3). This performance compares favourably to that of sophisticated infrared cameras, such as the one used in this work (3.0–5.0 μm wavelength, 640 × 512 pixels, 14 bits per pixel; Santa Barbara Focalplane Array, Lockheed Martin), which has a measured sensitivity of ∼24 mK (2 Hz sampling rate, $n = 300$; Supplementary Fig. S2f). We detected no hysteresis, within uncertainties, in the response of the sensors (Supplementary Fig. S4). Details of the set-up, calibration procedure and addressing schemes are given in Supplementary Note S3. Shown mounted on a human wrist in Fig. 2b, the epidermal sensor arrays reveal a spatial map of temperature (right) that matches well with the image obtained by the infrared camera (left). The scalability of the procedures for microfabrication provides straightforward routes to improved spatial resolution. The numbers of independently addressable sensors can be increased with multiplexing schemes that use the PIN diodes as switching elements. Figure 2d shows a temperature map (right) of a thin film copper heater, obtained with a PIN system (left).

The extremely thin and compliant construction of these devices provides important benefits. The first relates to mechanics. Here, the skin-like properties facilitate robust bonding to the skin without irritation, and enable effective isolation of the sensors/actuators from applied strain. This latter aspect is important because strain can change both the resistances and the turn-on voltages of the TCR and PIN sensors, respectively, in ways that could frustrate interpretation of the measurements. The open mesh, serpentine layouts, the neutral mechanical plane construction and the ultrathin device dimensions act together to minimize local strains on the sensors/actuators, even under relatively large system-level deformations. Motions of human skin involve a combination of wrinkling and stretching, to enable overall deformations of up to 100% in areas such as knees and elbows. The skin itself has a linear response to tensile strain up to ∼15%, nonlinear to ∼30%, and rupture at >30% (ref. 3), depending on factors including age and sun exposure[4]. Strain induced by wrinkling

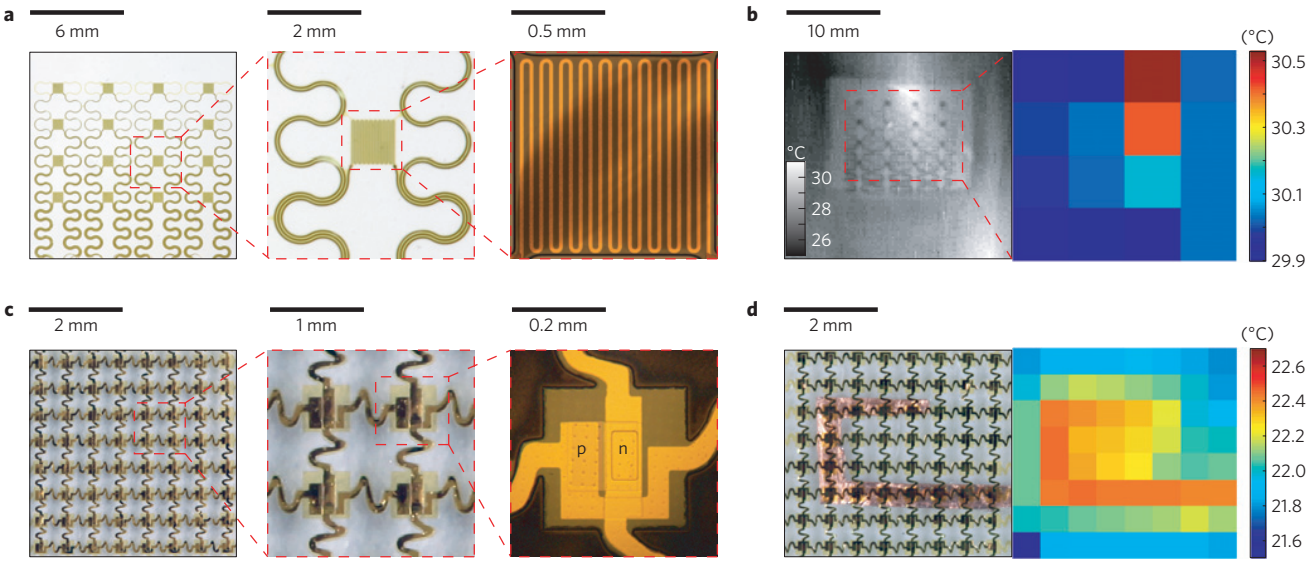


**Figure 2 | Functional demonstrations of epidermal temperature sensors and heaters. a**, Optical images of a 4 × 4 TCR sensor array integrated on a thin elastomeric substrate with magnified views of a single sensor. **b**, Infrared image of a similar device mounted on the skin of the human wrist (left) and map of temperature (right), where each pixel represents the reading of one sensor in the array. **c**, Optical images of a 8 × 8 Si nanomembrane diode sensor array integrated on a thin elastomeric substrate with magnified views of a single sensor. **d**, Optical image of a similar device mounted on a heated Cu element (left) and measured distribution of temperature (right).

can be well accommodated by the thin, neutral mechanical plane device designs. Tensile strains are relieved through microscale buckling and twisting of interconnect lines within the open mesh, serpentine layouts. Finite-element analysis (FEA) and experimental results (Supplementary Fig. S5) show, for example, that for a TCR device under a uniaxial strain of 10%, the average strains developed at the sensors/actuators are <0.02%, corresponding to <50 mK shift in the apparent temperature (Supplementary Note S4). Similar FEA on PIN systems (Supplementary Note S4) indicates maximum principal strains <0.55% (Supplementary Fig. S6). In many practical cases, modest changes associated with these small strains can be eliminated with signal processing that exploits differences between characteristic frequencies associated with motion and changes in temperature.

The second consideration relates to thermal loading and response times, where the extremely low thermal masses (Supplementary Note S5) of the devices and their high degrees of water/gas permeability (Supplementary Note S6) are advantageous. For the case of devices laminated directly onto the skin with no elastomeric backing (Fig. 1a), the calculated thermal mass per unit area is 150 μJ cm$^{-2}$ K$^{-1}$, which is the equivalent thermal mass per unit area of a layer of skin with thickness <500 nm, depending on hydration level. The addition of an elastomeric backing layer with thickness ~50 μm, which provides support for repeated application and removal of devices, raises the thermal mass per unit area to 7.2 mJ cm$^{-2}$K$^{-1}$, which is equal to <25 μm of skin. Furthermore, the thermal inertia, a measure of the resistance of a system to changes in temperature, of the elastomer system is ~500 W s$^{1/2}$ m$^{-2}$ K$^{-1}$, which is smaller than the value, 1,000–2,000 W s$^{1/2}$ m$^{-2}$ K$^{-1}$, for the skin itself[5,6]. As a result, the sensor system can respond rapidly to changes in skin temperature. Test experiments (Supplementary Fig. S7) involving application of a heated droplet of glycol on a sensor reveal response times (~5 ms) that are far faster than any known physiological thermal process measurable at the surface of the skin. Analytical models quantitatively reproduce these time dynamics (Supplementary Note S7), thereby providing guidelines for optimized designs. For example, the polyimide encapsulation layers play key roles: increasing the thickness from 3.6 to 6.0 μm increases the response time from 3.7 to 13.1 ms. The combined effects of this small thermal mass and the permeability of the thin silicone substrates minimize physiological impacts. Temperatures measured with the infrared camera on the palm near a sensor device and directly underneath it (Supplementary Fig. S8a,b) show minimal differences. The effect of the system on skin hydration (Supplementary Fig. S8c) is also small, corresponding to an increase in relative skin hydration of <6% after 3 h of continuous use, as measured by a commercial moisture metre (Delfin MoistureMeterSC). Experiments conducted under conditions of profuse sweating demonstrate a situation that requires devices with no elastomeric backing to avoid disrupting natural processes. Devices with no elastomeric backing show no significant effect on skin temperature during profuse sweating, whereas devices with an elastomeric backing result in small temperature increases, <2 °C, directly beneath the device following high-intensity exercise (Supplementary Fig. S9).

Figure 3 summarizes results of measurements with a TCR device on the palm during applications of mental and physical stimuli. An immobilized configuration enables comparison to measurements with infrared images collected directly through the transparent regions of the device and in adjacent areas. The mental stimulus experiments involved 30 min of rest, followed by a series of mental math problems involving simple operators such as subtraction and division. Measurements of temperature from a representative sensor in the array and the results of spatially averaging data from a neighbouring region in the infrared image are shown in Fig. 3b. In the period before the mental stimulus, the data show clear temperature fluctuations of 0.1–1.0 °C at frequencies of 0.005–0.05 Hz. Previous studies have indicated that skin on the palm has fluctuations in blood perfusion in this frequency regime due to the sympathetic activity of arteriovenous anastomoses[7–10]. The remarkable level of agreement between the various measurements throughout this experiment establishes the precision and the absence of any effects of the device on natural thermal processes. Physical stimulus, involving gently rubbing together two fingers on the hand opposite to the one with the sensor, leads to qualitatively similar behaviours, with similar levels of agreement (Supplementary Fig. S3c).

The low-frequency oscillations evident in the data of Fig. 3d have diagnostic value for conditions such as congestive heart

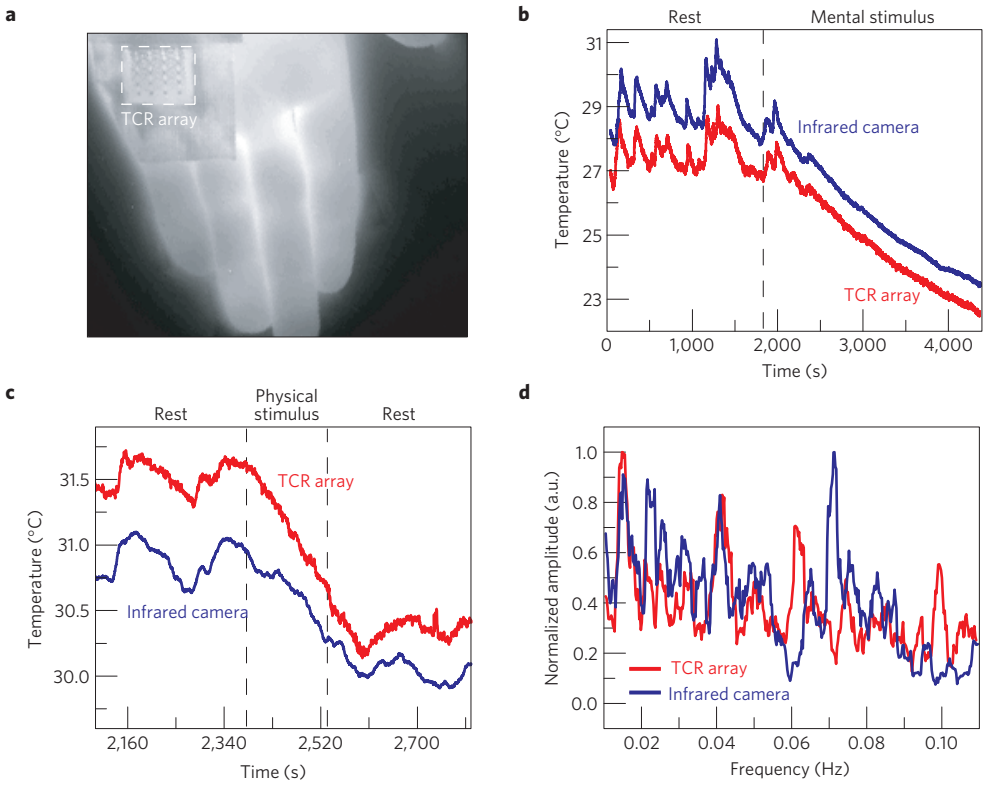


**Figure 3 | Epidermal electronic evaluations of skin temperature at rest and during mental and physical stimulation. a**, Infrared image of a 4 × 4 TCR sensor array mounted on the palm during stimulus experiments. **b**,**c**, Temperature of the palm measured with an infrared camera (blue) and a sensor array (red, offset for clarity) during mental (**b**) and physical stimulus tests (**c**) . **d**, Normalized Fourier transform of temperature measured on the forearm using a TCR sensor array (red), and using infrared camera evaluation through a transparent region of the array (blue). Both measurements show prominent peaks around 0.01 and 0.04 Hz.

disease and tissue hypoxia[11], and disturbances in skin blood flow may reflect functional changes due to disease in other important organ systems[12]. As small skin temperature changes correlate with tissue blood flow[13], they can serve as naturally occurring markers for monitoring periodic contraction and dilation of the vessels (vasomotion). Previous studies of oscillatory behaviour in blood flow at low frequencies suggest correlations to local vasomotions controlled by endothelium-derived hyperpolarizing factor (0.005–0.0095 Hz), rate of endothelial release of nitric oxide (0.0095–0.02 Hz), and sympathetic activity (0.02–0.06 Hz; ref. 14.) Continuous temperature measurements on the forearm during a 60 min rest period demonstrate capabilities in this context (Fig. 3d). Here, the low-frequency power spectra of temperatures from a TCR device and the infrared camera exhibit peaks at ∼0.01 Hz and ∼0.04 Hz, probably corresponding to the types of vasomotion described above. Further information and results of control experiments are given in Supplementary Fig. S8d and Note S8.

In addition to use as passive monitors of natural processes, these sensors can measure time-dynamic changes associated with externally stimulated events. Figure 4 illustrates a cardiovascular screening procedure[15,16] as an example of vasoconstrictive and vasodilative reactivity, where the vasculature adjusts blood flow through changes in vessel diameter in response to physiological stimuli[17]. Here, the device measures the temperature above the ulnar artery as part of a reactive hyperaemia protocol in which blood flow of the entire upper extremity is temporally occluded by a pressure cuff on the upper arm, and then the pressure is released. During the occlusion, the temperature of the skin (right above the ulnar artery) decreases markedly owing to lack of incoming blood flow and loss of heat to the environment. After the release of the occlusion, an overshoot in temperature above the baseline level may occur because of an increase in blood flow above the initial value. Studies have shown that the extent of vasodilation[18], maximal percentage increase in blood flow rate after occlusion[16], and duration of reactive hyperaemia[15] are valuable early indicators of the presence of cardiovascular risk factors. For example, the duration of reactive hyperaemia (defined as the time period between the release of occlusion and the return of blood flow to within 5% of the baseline value) was shown to be significantly lower in patients with hypercholesterolemia, diabetes mellitus, or in those who were smokers, as compared with healthy controls (80–95 s for those positive for risk factors as compared with 105–120 s for healthy controls)[15], and the incidence of death due to cardiovascular events was shown to be significantly less likely in patients with a maximal blood flow rate $>105\,\mathrm{cm\,s^{-1}}$ in the brachial artery during reactive hyperaemia as opposed to patients with smaller increases[16]. The responses of sensors across the array vary widely (Fig. 4c) owing to the localized thermal effect of the hyperaemic response of the ulnar artery, confirmed by the infrared image (Fig. 4b). The use of the spatial mapping array allows for useful measurement of the reactive hyperaemia response without precise placement of a single element above the artery. A thermal model of the human wrist (Supplementary Note S9 and Fig. S10) that considers the various tissues surrounding the ulnar artery, and quantitatively characterizes the heat exchange between the blood flow and the surrounding tissues, enables conversion of the measured changes in temperature (Fig. 4d, top) into changes in blood flow rate (Fig. 4d, bottom). The temporal variation of flow during the experiment can be approximated with a piecewise, exponential-type function, corresponding to the stages of pre-occlusion, vascular occlusion, and reperfusion after cuff pressure release[19,20]. The parameters characterizing this function

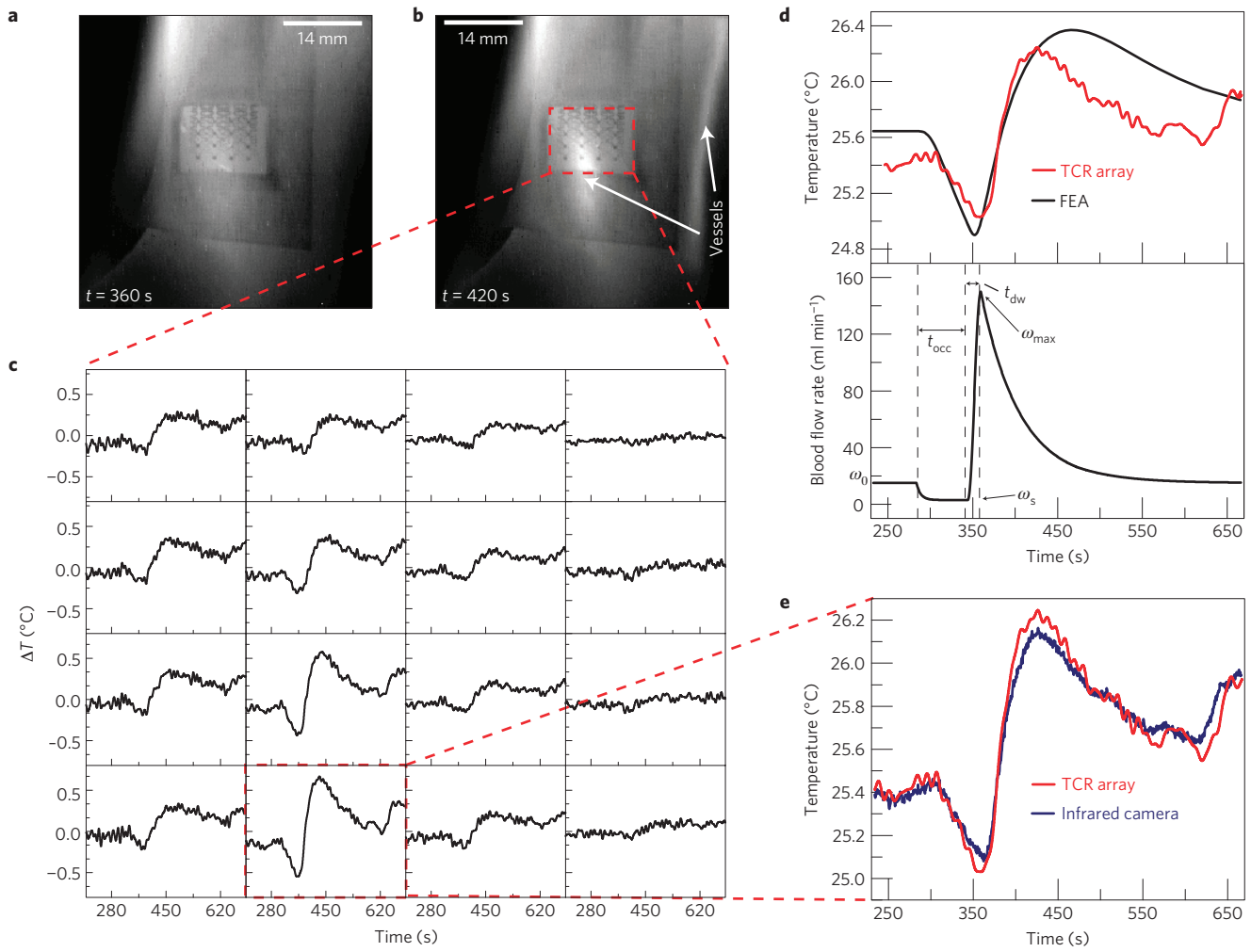


**Figure 4 | Epidermal electronics for a reactive hyperaemia test. a**,**b**, Infrared image of a 4 × 4 TCR sensor array on the wrist during an occlusion test at $t = 360$ s (corresponding to the end of a 60 s period of occlusion, during which there is minimal blood flow; **a**) and $t = 420$ s (corresponding to the peak in temperature rise after releasing the occlusion; **b**). **c**, Measured temperature changes during occlusion ($t = 300$–$360$ s) and after occlusion ($t = 360$–$660$ s) recorded by each of the 16 sensors in the 4 × 4 TCR sensor array. **d**, FEA of the temperature rise at the surface of the skin above the ulnar artery during the occlusion experiment as compared with experimental data (top) and blood flow rate through the ulnar artery used in the FEA (bottom). The key parameters characterizing the temporal variation of blood flow rate include: the occlusion time ($t_{occ}$) = 60 s as used in the experiment; time-to-peak-flow ($t_{dw}$) = 15 s; baseline flow rate ($\omega_0$) = 15 ml min$^{-1}$; occluded flow rate ($\omega_s$) = 3 ml min$^{-1}$; peak flow rate ($\omega_{max}$) = 150 ml min$^{-1}$. **e**, Temperature measured by the single sensor that showed the largest temperature change during the occlusion test.

are determined by the corresponding stages of temperature–time profiles derived from experimental measurement. Figure 4d demonstrates that the calculated temperature history using the thermal model can accurately account for the experimental results. For vessel diameters and depths that lie within reported ranges (Supplementary Note S9), the peak blood flow velocity after occlusion is calculated to be 98 cm s$^{-1}$, which represents a tenfold increase over the baseline of 9.8 cm s$^{-1}$, with a reactive hyperaemia duration of 127 s. These values match well with the literature[15,16] for a person with low cardiovascular risk.

In comparison with conventional, point-contact sensors and infrared cameras, the technologies reported here offer an additional option for delivering precise levels of heating to the surface of the skin. An important example of the expanded capabilities that follow is a strategy for determining the local thermal conductivity. This parameter is of interest partly because it is known to serve as a useful proxy for free-water content[5], as a simple methodology to monitor skin hydration and perspiration. In this mode, the temperature of a sensor element is measured during the application of constant current over two seconds, to create a small temperature rise (<2 °C) on the skin. The thermal conductivity ($k$) of the skin is determined through a modification of the transient plane heat source method[21] and standardized ISO-22007-2-2008 procedure, as outlined in Supplementary Note S10. Calibration can be performed with deionized water and ethylene glycol, and verified in four water/glycol mixtures (Fig. 5a). Figure 5c shows the temperature rise of a sensor element in contact with deionized water, air and the human forearm during measurement. A minimal power level of 1 mW, applied for two seconds, is required to obtain accurate measurements, as indicated by the large error bars associated with measurements with powers <1 mW in Fig. 5d. The characteristic depth of measurement, discussed in Supplementary Note S10, is approximately 500 μm. The simple correlation between the maximum rise in temperature and the reported thermal conductivity, shown as a shaded region in Fig. 5c and quantitatively in Fig. 5e, additionally provides a means to verify adequate sensor–skin thermal contact during long-term clinical monitoring. Figure 5e indicates excellent correspondence between thermal conductivity and hydration determined with a moisture meter (Delfin MoistureMeterSC) that uses electrical impedance.

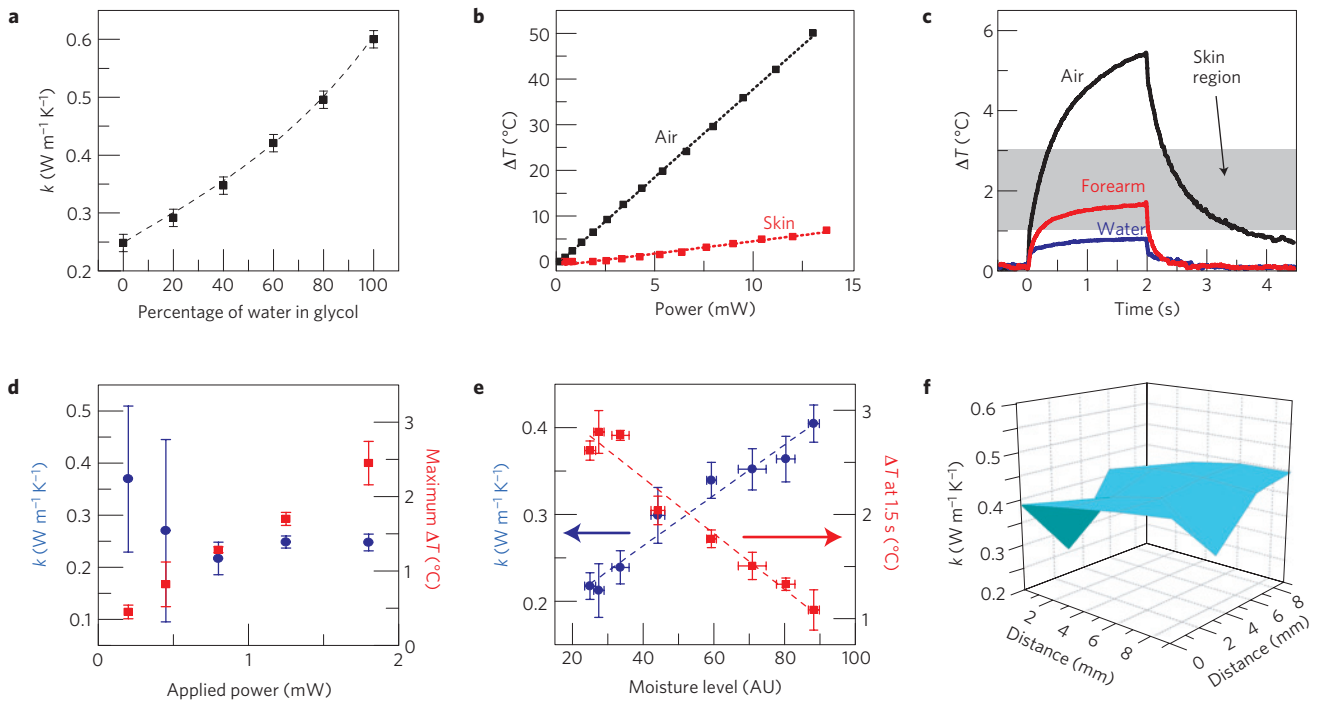


**Figure 5 | Epidermal electronics configured for evaluating skin hydration and thermal conductivity. a**, Thermal conductivity of water/ethylene glycol solutions as measured by a TCR heater/temperature sensor (points) and reported in the literature (dotted line). Error bars represent average standard deviations of six different ethylene glycol/water solution data sets, ten measurements each. **b**, Temperature rise as a function of Joule heating rate provided by a TCR heater/temperature sensor on an elastomeric backing, laminated onto the skin (red) and free-standing in air (black) **c**, Representative temperature rise during a 2 s period of heating on the elastomeric backing free-standing in air, laminated onto the human forearm, and with a drop of water on top. When laminated on skin, the temperature rise typically falls within the shaded region. **d**, Measured thermal conductivity (blue) and maximal temperature rise of the heater (red) as a function of Joule heating rate provided by a TCR heater/temperature sensor from $t = 0$–2 s. Error bars represent standard deviations over ten measurements. The results indicate that a power of only ~1 mW enables reasonable signal to noise. **e**, Thermal conductivity (blue) and temperature rise at $t = 1.5$ s (red) as a function of skin hydration as measured with a commercial moisture meter (Delfin). The points and dotted lines represent measured data and modelling, respectively. Error bars represent standard deviations over ten measurements. The applied power in this case was 1.8 mW. **f**, Spatial mapping of thermal conductivity on the forearm, measured using a 4 × 4 TCR heater/sensor array.

Figure 5f demonstrates the use of this technique to generate a spatial map of thermal conductivity of the skin, by individual control of the actuators. Advantages of thermal measurements of hydration compared with those based on capacitance or impedance include the ability to isolate the electronics from the skin and to measure both temperature and thermal conductivity with a single system.

The results presented here demonstrate that unusual combinations of materials and device components in stretchable electronic systems can, when implemented with advanced modelling and analysis techniques, enable versatile, precision capabilities in thermal characterization of the skin. Several key features of operation suggest potential for practical use outside hospital settings, to provide real-time, clinical quality data for continuous health/wellness assessment. The microfabrication techniques used for these devices and the multiplexed schemes for addressing the sensors/actuators in them both scale in ways that create opportunities for substantially increased spatial resolution, with potential for monitoring of blood perfusion or localized thermogenesis associated with inflammatory events in tissues, as well as vascular tone and reactivity within well-defined vasculature territories, including capillary beds. Ongoing efforts into wireless device implementation will allow application of the techniques presented here to long-term studies with continuous precision thermal monitoring. Adapted versions of this technology may also allow intraoperative application to surgically exposed organs, including observation of high-frequency changes in vascular flow (for example, influenced by cardiac and respiratory rates). Furthermore, the use of combined temperature sensing and microheating arrays in clinical research may create principally new diagnostic and therapeutic approaches for medicine. Use of local heating to create skin temporal windows for localized drug delivery through targeted microvascular territory[22], non-invasive glucose monitoring[23], or local nutrient delivery critical for rapid, infection-resistant wound healing[24] represent additional possibilities of interest.

## Methods

**Fabrication of TCR devices.** The fabrication, detailed in Supplementary Note S1, began with spin-coating of a thin film of polyimide (~1.2 μm, Sigma Aldrich) on a sacrificial layer of poly(methylmethacrylate) (100 nm, MicroChem). Metal-evaporation (Cr/Au, 5 nm/50 nm), photolithography and wet-etching steps defined serpentine-shaped TCR sensors. Additional polyimide spin-coating, oxygen reactive ion etching and metal deposition for contacts and interconnects completed the array, which was then transferred to a thin silicone support and bonded to a thin, flexible cable for external connection.

**Fabrication of PIN devices.** The fabrication, detailed in Supplementary Note S2, began by defining n- and p-doped regions on a silicon on insulator (320 nm Si on buried oxide) wafer. The doped regions were then transfer printed onto a Si wafer coated with poly(methylmethacrylate) and polyimide. Metal-evaporation, photolithography, chemical vapour deposition and wet-etching steps defined metallization layers. Additional polyimide spin-coating, oxygen reactive ion etching and metal deposition for contacts and interconnects completed the array, which was then transferred to a thin silicone support and bonded to a thin, flexible cable for external connection.

**Thermal oscillation test.** A volunteer (male, 28 years old) reclined in a chair with his left forearm gently secured to the armrest using Velcro strips to reduce

movement. A TCR device was placed on the ventral side of the left forearm and brought into thermal contact with a puff of compressed air. The infrared camera was placed 41 cm from the subject's left forearm, focused on the TCR device. The lights were then turned off ($t = 0$) and the subject was instructed to relax for 60 min. At $t = 60$ min the period of data acquisition ended.

**Mental stimulus test.** A volunteer (male, 28 years old) reclined in a chair with his left forearm secured gently to the armrest using Velcro strips to reduce movement. A TCR device was placed on the ventral side of the left forearm and brought into thermal contact with a low-velocity puff of compressed air. The infrared camera was placed 41 cm from the subject's left forearm, focused on the TCR device. The lights were then turned off ($t = 0$) and the subject was instructed to relax for 30 min. At $t = 30$ min an alarm sounded, and the subject was given a further 10 min of relaxation. At $t = 40$ min the subject began a series of mental arithmetic lasting 30 min. At $t = 70$ min the period of data acquisition ended.

**Physical stimulus test.** A volunteer (male, 28 years old) reclined in a chair with his left forearm secured gently to the armrest using Velcro strips to reduce movement. A TCR device was placed on the palm of the left hand and brought into thermal contact with a puff of compressed air. The infrared camera was placed 41 cm from the subject's left palm, focused on the palm at the location of the TCR device. The lights were then turned off ($t = 0$) and the subject was instructed to relax for 30 min. At $t = 30$ min an alarm sounded, and the subject was given a further 10 min of relaxation. At $t = 40$ min the subject began to rub the fingers of his right hand together for a period of 2 min. At $t = 42$ min the subject ceased rubbing and attempted to relax for a further 20 min. At $t = 62$ min the period of data acquisition ended.

**Reactive hyperaemia test.** A volunteer (male, 28 years old) reclined in a chair with his left forearm secured gently to the arm rest using Velcro strips to reduce movement. A pressure cuff was secured around the subject's left bicep. A TCR device was placed on the skin of the left wrist, volar aspect, approximately above the ulnar artery and brought into thermal contact with a puff of compressed air. The infrared camera was placed 41 cm from the subject's left wrist, focused on the location of the TCR device. The lights were then turned off ($t = 0$) and the subject was instructed to relax for 5 min. At $t = 5$ min the pressure cuff was inflated to a pressure of 250 mm Hg for a period of 1 min. At $t = 6$ min the pressure in the cuff was released. The subject was instructed to relax for 24 min. At $t = 30$ min the period of data acquisition ended.

**Thermal conductivity and hydration measurements.** Thermal conductivity was determined by analysing the temperature rise data from sensor elements during a 2 s period of heating. Each measurement occurred in three stages of measuring the voltage drop during a period of constant current using a Gamry Instruments Reference 600 Potentiostat: application of 100 μA for 2 s, switching to 1.5 mA for 2 s (heating), and switching to 100 μA for 2 s. This measurement was performed ten times on a single sensor, and the temperature rise data were analysed according to the transient plane source method, as outlined in Supplementary Note S10.

Received 13 March 2013; accepted 8 August 2013; published online 15 September 2013; corrected after print 26 September 2013

## References


1. Wang, S. D. *et al.* Mechanics of epidermal electronics. *J. Appl. Mech.-T. ASME* **79,** 031022 (2012).
2. Kim, D. H. *et al.* Epidermal electronics. *Science* **333,** 838–843 (2011).
3. Arumugam, V., Naresh, M. D. & Sanjeevi, R. Effect of strain rate on the fracture behaviour of skin. *J. Biosci.* **19,** 307–313 (1994).
4. Agache, P. G., Monneur, C., Leveque, J. L. & De Rigal, J. Mechanical properties and Young's modulus of human skin *in vivo*. *Arch. Dermatol. Res.* **269,** 221–232 (1980).
5. Cohen, M. L. Measurement of thermal-properties of human-skin—review. *J. Invest. Dermatol.* **69,** 333–338 (1977).
6. Hassan, M. & Togawa, T. Observation of skin thermal inertia distribution during reactive hyperaemia using a single-hood measurement system. *Physiol. Meas.* **22,** 187–200 (2001).
7. Thoresen, M. & Walloe, L. Skin blood-flow in humans as a function of environmental-temperature measured by ultrasound. *Acta Physiol. Scand.* **109,** 333–341 (1980).
8. Lossius, K., Eriksen, M. & Walloe, L. Fluctuations in blood-flow to acral skin in humans—connection with heart-rate and blood-pressure variability. *J. Physiol.* **460,** 641–655 (1993).
9. Crandall, C. G., Meyer, D. M., Davis, S. L. & Dellaria, S. M. Palmar skin blood flow and temperature responses throughout endoscopic sympathectomy. *Anesth. Anal.* **100,** 277–283 (2005).
10. Jansky, L. *et al.* Skin temperature changes in humans induced by local peripheral cooling. *J. Therm. Biol.* **28,** 429–437 (2003).
11. Bernjak, A., Clarkson, P. B., McClintock, P. V. & Stefanovska, A. Low-frequency blood flow oscillations in congestive heart failure and after beta1-blockade treatment. *Microvasc. Res.* **76,** 224–232 (2008).
12. Holowatz, L. A., Thompson-Torgerson, C. S. & Kenney, W. L. The human cutaneous circulation as a model of generalized microvascular function. *J. Appl. Physiol.* **105,** 370–372 (2008).
13. Gorbach, A. M. *et al.* Infrared imaging of nitric oxide-mediated blood flow in human sickle cell disease. *Microvasc. Res.* **84,** 262–269 (2012).
14. Kvandal, P. *et al.* Low-frequency oscillations of the laser Doppler perfusion signal in human skin. *Microvasc. Res.* **72,** 120–127 (2006).
15. Ishibashi, Y. *et al.* Short duration of reactive hyperemia in the forearm of subjects with multiple cardiovascular risk factors. *Circ. J.* **70,** 115–123 (2006).
16. Huang, A. L. *et al.* Predictive value of reactive hyperemia for cardiovascular events in patients with peripheral arterial disease undergoing vascular surgery. *Arterioscler. Thromb. Vasc.* **27,** 2113–2119 (2007).
17. Nordin, M. Sympathetic discharges in the human supraorbital nerve and their relation to sudo- and vasomotor responses. *J. Physiol.* **423,** 241–255 (1990).
18. Celermajer, D. S. *et al.* Non-invasive detection of endothelial dysfunction in children and adults at risk of atherosclerosis. *Lancet* **340,** 1111–1115 (1992).
19. Akhtar, M. W., Kleis, S. J., Metcalfe, R. W. & Naghavi, M. Sensitivity of digital thermal monitoring parameters to reactive hyperemia. *J. Biomech. Eng.* **132,** 051005 (2010).
20. Deshpande, C. *Thermal Analysis of Vascular Reactivity*. MS thesis, Texas A&M Univ. (2007).
21. Gustafsson, S. E. Transient plane source techniques for thermal conductivity and thermal diffusivity measurements of solid materials. *Rev. Sci. Instrum.* **62,** 797–804 (1991).
22. Park, J. H., Lee, J. W., Kim, Y. C. & Prausnitz, M. R. The effect of heat on skin permeability. *Int. J. Pharm.* **359,** 94–103 (2008).
23. Paranjape, M. *et al.* A PDMS dermal patch for non-intrusive transdermal glucose sensing. *Sens. Actuat. A* **104,** 195–204 (2003).
24. Ikeda, T. *et al.* Local radiant heating increases subcutaneous oxygen tension. *Am. J. Surg.* **175,** 33–37 (1998).


## Acknowledgements

This material is based on work supported by the National Science Foundation under Grant No. DGE-1144245, Grant No. ECCS-0824129 and through the Materials Research Laboratory and Center for Microanalysis of Materials at the University of Illinois at Urbana-Champaign. J.A.R. acknowledges financial support through a National Security Science and Engineering Faculty Fellowship. The work on silicon nanomembranes was financially supported by a MURI grant from the Air Force Office of Scientific Research. This research was supported in part by the Intramural Research Program of NIBIB, NIH. The authors would like to thank H. Eden for his invaluable critique and insightful comments during preparation of this manuscript.

## Author contributions

A.P.B., R.C.W., A.B., A.M.G. and J.A.R. designed the experiments. A.P.B., R.C.W., K.J.Y., Y-S.K., W-H.Y. and J.S.P. carried out the fabrication. A.P.B., R.C.W., A.B., A.M.G. and J.A.R. carried out experimental validation and data analysis. Y.Z., Z.B., J.S., Y.L. and Y.H. contributed to the thermal modelling of sensor response time and reactive hyperaemia. H.C., M.S., Z.L. and Y.H. contributed to the mechanical modelling of strain. R.C.W., A.P.B., A.B., Y.Z., H.C., Z.B., Y.H., A.M.G. and J.A.R. co-wrote the paper.

## Additional information

Supplementary information is available in the online version of the paper. Reprints and permissions information is available online at www.nature.com/reprints. Correspondence and requests for materials should be addressed to J.A.R.

## Competing financial interests

The authors declare no competing financial interests.

ERRATUM

# Ultrathin conformal devices for precise and continuous thermal characterization of human skin

R. Chad Webb, Andrew P. Bonifas, Alex Behnaz, Yihui Zhang, Ki Jun Yu, Huanyu Cheng, Mingxing Shi, Zuguang Bian, Zhuangjian Liu, Yun-Soung Kim, Woon-Hong Yeo, Jae Suk Park, Jizhou Song, Yuhang Li, Yonggang Huang, Alexander M. Gorbach and John A. Rogers

*Nature Materials* **12,** 938–944 (2013); published online 15 September 2013; corrected after print 26 September 2013.

In the version of this Article originally published, in Fig. 3b,c the labels at the top of the graphs were missing. This error has been corrected in the HTML and PDF versions of the Article.

nature materials

SUPPLEMENTARY INFORMATION

DOI: 10.1038/NMAT3755

# Ultrathin conformal devices for precise and continuous thermal characterization of human skin

R. Chad Webb[1†], Andrew P. Bonifas[1†], Alex Behnaz[2], Yihui Zhang[3,4], Ki Jun Yu[5], Huanyu Cheng[4], Mingxing Shi[6], Zuguang Bian[4,7], Zhuangjian Liu[8], Yun-Soung Kim[1], Woon-Hong Yeo[1], Jae Suk Park[5], Jizhou Song[9], Yuhang Li[4], Yonggang Huang[4], Alexander M. Gorbach[2], John A. Rogers[1*]

[1]Department of Materials Science and Engineering, University of Illinois at Urbana-Champaign, Urbana, IL 61801, USA
[2]National Institute of Biomedical Imaging and Bioengineering, National Institutes of Health, Bethesda, MD 20892, USA
[3]Center for Mechanics and Materials, Tsinghua University, Beijing 100084, P.R. China
[4]Department of Civil and Environmental Engineering and Department of Mechanical Engineering, Northwestern University, Evanston, IL 60208, USA
[5]Department of Electrical and Computer Engineering, University of Illinois at Urbana-Champaign, Urbana, IL 61801, USA
[6]School of Mechanics and Engineering, Southwest Jiaotong University, Chengdu 610031, P.R. China
[7]Ningbo Institute of Technology, Zhejiang University, Ningbo 315100, P.R. China
[8]Institute of High Performance Computing, 1 Fusionopolis Way, #16-16 Connexis, Singapore 138632
[9]Department of Mechanical and Aerospace Engineering, University of Miami, Coral Gables, Florida 33146, USA

[†]These authors contributed equally to this work

*To whom correspondence should be addressed: E-mail: jrogers@illinois.edu

DOI: 10.1038/NMAT3755

## Supplementary Note 1: Fabrication procedure for 4 x 4 TCR sensor arrays

### *Prepare polymer base layers*

1. Clean a 3" Si wafer (Acetone, IPA -> Dry 5 min at 110 °C).
2. Spin coat with PMMA (poly(methyl methacrylate), spun at 3,000 rpm for 30 s).
3. Anneal at 180 °C for 1 min.
4. Spin coat with polyimide (PI, poly(pyromellitic dianhydride-co-4,4′ -oxydianiline), amic acid solution, Sigma-Aldrich, spun at 4,000 rpm for 30 s).
5. Anneal at 110 °C for 30 s.
6. Anneal at 150 °C for 5 min.
7. Anneal at 250 °C under vacuum for 1 hr.

### *Deposit first metallization*

8. E-beam 5/40 nm Cr/Au.
9. Pattern photoresist (PR; Clariant AZ5214, 3000 rpm, 30s) with 365 nm optical lithography through iron oxide mask (Karl Suss MJB3).
   Develop in aqueous base developer (MIF 327).
10. Etch Au with TFA Au etchant (Transene).
11. Etch Cr with CR-7 Cr Mask Etchant (Cyantek).
12. Remove PR w/ Acetone, IPA rinse.
13. Dry 5 min at 150 °C.

### *Isolate first metallization and pattern via holes*

14. Spin coat with PI.
15. Anneal at 110 °C for 30 s.
16. Anneal at 150 °C for 5 min.
17. Anneal at 250 °C under vacuum for 1 hr.
18. Pattern photoresist (PR; Clariant AZ4620, 3000 rpm, 30s;) with 365 nm optical lithography through iron oxide mask (Karl Suss MJB3).
    Develop in aqueous base developer (AZ 400K, diluted 3:1).
19. Reactive ion etch (RIE; March CS-1701, 50 mTorr, 20 sccm O2, 150 W, 35 min).

### *Deposit second metallization*

20. E-beam 5/200 nm Cr/Au.
21. Pattern PR AZ5214.
22. Etch Au with TFA Au etchant.
23. Etch Cr with Cr Mask Etchant.
24. Remove PR w/ Acetone, IPA rinse.
25. Dry 5 min at 150 °C.

***Isolate entire device***

26. Spin coat with PI.
27. Anneal at 110 °C for 30 s.
28. Anneal at 150 °C for 5 min.
29. Anneal at 250 °C under vacuum for 1 hr.
30. Pattern PR AZ4620.
31. RIE (50 mTorr, 20 sccm O2, 150 W, 35 min).

***Release and transfer***

32. Release w/ boiling Acetone.
33. Transfer to PDMS stamp.
34. E-beam 3/30 nm Ti/SiO2.
35. Transfer to ~50 μm silicone sheet.
36. Bond thin, flexible cable (Elform, HST-9805-210) using hot iron with firm pressure

**Supplementary Note 2: Fabrication procedure for 8 x 8 PIN sensor arrays**

***p+ doping***

1. Clean a 320 nm SOI wafer (acetone, IPA, water, drying at 110°C for 5 min).
2. Clean by Buffer Oxide Etch (BOE) 6:1 for 1 min.
3. Deposit Plasma Enhanced Chemical Vapor Deposition (PECVD; Plasmatherm SLR730) $SiO_2$ 900 nm.
4. Clean the wafer (acetone, IPA, water, drying at 110°C for 5min).
5. Treat with HMDS for 3 min.
6. Pattern PR (p+ doping).
7. Anneal at 110°C for 5 min.
8. Etch oxide in RIE ($CF_4$: 40 sccm, $O_2$: 1.2 sccm, 150W, 59 mTorr) for 30 min.
9. Etch residual oxide in BOE ($NH_4F$:HF=10:1) for 2 min.
10. Remove PR by acetone
11. Clean by RCA 1 and RCA 2 for 10 min each
12. Dip in BOE for 10 sec
13. Expose to diffusive boron source at 1000°C for 25 min.
14. Clean the processed wafer (HF 1min, RCA 1 for 10 min, RCA 2 for 10 min BOE 1 min).

***n+ doping***

15. Deposit PECVD SiO2 500 nm.
16. Clean the wafer (acetone, IPA, water, drying at 110°C for 5 min).

DOI: 10.1038/NMAT3755

17. Treat with HMDS for 3 min.
18. Pattern PR (n+ doping).
19. Anneal at 110°C for 5 min.
20. Etch oxide in RIE ($CF_4$: 40 sccm, $O_2$: 1.2 sccm, 150W, 59 mTorr) for 20 min.
21. Etch residual oxide in BOE ($NH_4F$:HF=10:1) for 1.5 min.
22. Remove PR by acetone
23. Clean by RCA 1 and RCA 2 for 10 min each
24. Dip in BOE for 10 sec
25. Expose to diffusive phosphorus source at 1000°C for 7 min.
26. Clean the processed wafer (HF 1min, RCA 1 for 10min, RCA 2 for 10 min BOE 1 min).

***Oxide layer etching in SOI wafer***

27. Pattern PR (3 μm pitch dot patterns).
28. Etch silicon by RIE (50mTorr, 40sccm SF6, 100W, 1 min).
29. Etch buried oxide layer of SOI wafer via dot patterns in HF for 30 min.

***Substrate preparation***

30. Spin coat with PMMA on the substrate (additional wafer, 3000 rpm 30 s).
31. Anneal at 180 °C for 3 min.
32. Spin coat with PI (4000 rpm, 60 s).
33. Aneal at 110 °C for 40 s.

***Transfer printing***

34. Release Si layer with PDMS stamp from SOI wafer.
35. Print Si layer onto prepared substrate.
36. Anneal at 150°C for 4 min.
37. Remove PR by acetone and IPA.
38. Aneal at 250°C for 1 h under vacuum.

***Silicon Isolation***

39. Pattern PR.
40. Etch silicon by RIE (50 mTorr, 40 sccm $SF_6$, 100 W, 1 min)
41. Remove PR by acetone and IPA.

***Pattern 1st via hole***

42. Deposit PECVD $SiO_2$ 100 nm.
43. Pattern PR (holes).
44. Open via holes with BOE for 1 min.

45. Remove PR by acetone and IPA.

***Deposit 1st Metallization***

46. E-beam 10/100 nm Cr/Au.
47. Pattern PR.
48. Wet etch Cr/Au.
49. Remove PR by acetone and IPA.

***Isolate 1st layer and Pattern 2nd via hole***

50. Spin coat with PI (4000 rpm, 60 s).
51. Anneal at 110°C for 3min at 150°C for 10 min.
52. Anneal at 250°C for 2 h under vacuum.
53. Pattern PR.
54. Etch via holes by RIE ($O_2$: 20 sccm, 200W, 150 mTorr) for 10 min.
55. Remove PR by acetone and IPA.

***Deposit 2nd Metallization***

56. E-beam 10/700 nm Cr/Au.
57. Pattern PR.
58. Wet etch Cr/Au.
59. Remove PR by acetone and IPA.

***Isolate 2st layer and Pattern 3nd via hole***

60. Spin coat with PI (4000 rpm, 60 s).
61. Anneal at 110°C for 3 min at 150°C for 10 min.
62. Anneal at 250°C for 2 h under vacuum.
63. Pattern PR.
64. Etch via holes by RIE (20 sccm $O_2$, 200 W, 150 mTorr) for 10 min.
65. Remove PR by acetone and IPA.

***Deposit 3rd Metallization***

66. E-beam 10/300 nm Cr/Au.
67. Pattern PR.
68. Wet etch Cr/Au.
69. Etch 3rd PI layer by RIE (20 sccm $O_2$, 200 W, 150 mTorr) for 5 min.
70. Pattern PR for ACF opening.
71. Wet etch Cr/Au.
72. Remove PR by acetone and IPA.
73. Release and transfer

DOI: 10.1038/NMAT3755

74. Bond thin, flexible cable (Elform, HST-9805-210) using hot iron with firm pressure

**Supplementary Note 3: Temperature measurements and calibrations**

Temperature measurements of the TCR devices are recorded via a National Instruments PXI-6289 board with custom electronics programmed with LabVIEW software with all 16 channels recorded simultaneously at a 15 ms sampling time. The probe current employed to measure resistance was selected to be 160 μA to avoid self-heating of the sensors, confirmed to be less than 0.02 °C with IR thermometry, while maximizing signal to noise. A 16 bit A/D converter, an input range of ±200 mV, and a 160 μA probe current has 0.04 Ω bin sizes resulting in a bin size of 0.02 °C at our sampling frequency of 66.67 Hz. The sampling frequency was limited by the data transfer speed of the laptop computer.

Temperature sensor calibrations are performed by applying the devices to an aluminum plate, painted matte black, and set on a hot plate. For the TCR device, the hot plate is set to one of six temperature points from 25 °C – 50 °C, allowed to stabilize for 10 min, and then the resistances of all 16 sensors are recorded for 60 seconds. The temperature is recorded using an IR thermometer, and the resistance value for each sensor is given as the average of each sensor's 60 second recording. This measurement is repeated for a total of six temperature points from 25 °C – 50 °C and is used to generate the calibration curves shown in Supplementary Figure S2a. The 16 curves are separated into four groups of four, each group separated by a small resistance constant, due to the difference in interconnect length for each of the 4 rows. A typical value for the resistance change of a sensor due to temperature is 1.9 - 2 $\Omega \cdot °C^{-1}$, as shown in Supplementary Figure S2a. This resistance change corresponds to a TCR value of 2.5 x $10^{-3}$ $°C^{-1}$, which is lower than the reported bulk Au value of 3.7 x $10^{-3}$ $°C^{-1}$. Thin metallic layers typically have lower TCR compared to their bulk material owing to a large constituent of temperature independent resistance caused by surface scattering[1]. The generated calibration equation for each sensor is then applied to future measurements to convert resistance readings to temperature. Typical data points during a 150 s measurement period on the bench and on skin are shown in Supplementary Figure S2d-e, respectively. When data is averaged from 66.67 Hz to 2 Hz, which is shown in Supplementary Figure S2d-e, the standard deviations of the temperature readings over the 150 s periods are 0.012 °C and 0.021 °C for the sensor on the hot plate and on skin, respectively. If the data is averaged from 66.67 Hz to 0.5 Hz, the standard deviations drop to 0.008 °C and 0.014 °C on the hot plate and skin, respectively. It was observed that the absolute accuracy of the sensors would sometimes vary between experiments while maintaining the same temperature sensitivity, which would manifest itself in a constant offset in temperature reading. This is attributed to small variations in the contact resistance between the sensor contact

pads and heat bonded cable used to connect to the data acquisition system. Because the sensors rely on a measurement of voltage drop through the circuit, a change in the contact resistance of the wire leads should manifest as a constant offset in temperature reading. This change was typically <5 °C over a period of months, and could be alleviated by the use of 4-point resistance measurements, or wireless data transmission in the future. To account for the potential constant resistance offset, the temperature reading of each sensor was compared to the IR camera reading at a single instance in time, and the difference was applied as a constant to each sensor's calibration equation. This was deemed reasonable because the data of interest is precise temperature changes over time, as opposed to absolute temperature accuracy.

PIN devices were measured and calibrated in the same fashion as the TCR devices, but with a different data acquisition system. PIN diodes were measured using an Agilent 4155C parameter analyzer to measure the voltage drop at forward biased current levels of 10 μA and 20 μA, which show corresponding sensitivities of 2.34 $mV \cdot °C^{-1}$ and 2.44 $mV \cdot °C^{-1}$ respectively (Supplementary Fig. S2b-c). Individual diodes can be addressed in the array in a multiplexed format by picking the proper row and column external contacts to apply bias, allowing current to only flow through a single diode at any given time in a format that allows for rapid switching.

**Supplementary Note 4: Strain effects**

Finite element analysis (FEA) was used to study the effect of device strain on both the TCR and PIN based temperature sensors. For the TCR device, the sensors were assumed to be perfectly bonded to the elastomeric substrate for modeling purposes. An applied uniaxial strain of 10% was applied in the longitudinal direction at the upper end of the substrate while the lower end was clamped. The substrate was modeled by the hexahedron element C3D8R; the sensor arrays were modeled by the composite shell element S4R in the ABAQUS finite element program. The strains in the TCR elements in the longitudinal and horizontal directions shown in Supplementary Figure S5b-c indicate small variation across the width direction of each TCR element. Each TCR element can be taken as many small resistors connecting in parallel in the width direction followed by a series connection in the length direction. Small variation of the strain in the width direction allows us to approximate the parallel connection with an average calculation, which leads to a simplified expression of the relative resistance change $\Delta R/R = \left(1+\varepsilon_{length}\right)\Big/\left(1+\varepsilon_{width}\right)-1$, where $\varepsilon_{length}$ and $\varepsilon_{width}$ are the average strains in the length and width directions, respectively. This approximation gives the upper bound of the resistance change, which is confirmed with the comparison to the experiment as shown in Supplementary Figure 5d.

DOI: 10.1038/NMAT3755

Unlike TCR devices with increased interconnect lengths of progressive sensor rows, the PIN device appears in a periodic mesh layout, which simplifies our analysis to a unit cell containing only one diode in the finite element analysis. Periodic boundary conditions were applied to ensure that each unit cell neither overlaps nor form gaps with adjacent cells, while a uniaxial 10% strain was applied. Element type selections are the same as described in the analysis for TCR device. Because silicon diodes are off from the neutral mechanical plane of the device, bending was induced even though only uniaxial strain was applied, as supported by the strain profiles at the top and bottom surfaces of Si diode in Supplementary Figure S6.

**Supplementary Note 5: Thermal load on skin**

The thermal mass of the devices are determined for two practical constructions: with and without a 50 μm silicone supporting substrate. The devices have an overall aerial coverage of ~4 $cm^2$. The calculated thermal masses that follow are given as thermal mass per unit area of skin. The device construction for the TCR device contains approximately 120 $\mu g \cdot cm^{-2}$ of Au, 90 $\mu g \cdot cm^{-2}$ of PI, and, for the case with a 50 μm silicone backing, 5 $mg \cdot cm^{-2}$ of silicone support (calculated values). The material contributions to aerial thermal mass are: 15 $\mu J \cdot cm^{-2} \cdot K^{-1}$ from Au, 125 $\mu J \cdot cm^{-2} \cdot K^{-1}$ from PI, and 7 $mJ \cdot cm^{-2} \cdot K^{-1}$ from the silicone backing (calculate values). This resulting overall device aerial thermal masses are 150 $\mu J \cdot cm^{-2} \cdot K^{-1}$ for the case with no silicone support, and 7.2 $mJ \cdot cm^{-2} \cdot K^{-1}$ for the case of a 50 μm silicone support. The PIN system has a denser device coverage, with resulting aerial thermal mass of approximately 500 $\mu J \cdot cm^{-2} \cdot K^{-1}$ for the case with no silicone support, and 7.6 $mJ \cdot cm^{-2} \cdot K^{-1}$ for the case with the silicone support. The thermal mass of skin depends on the water content where thermal mass increases with skin hydration and water content[2]. For hydrated skin, the heat capacity is approximately 3.7 $J \cdot cm^{-3} \cdot K^{-1}$, and the device aerial thermal mass (no support) of 120 $\mu J \cdot cm^{-2} \cdot K^{-1}$ is equivalent to the aerial thermal mass of skin with a thickness of 320 nm (320 nm skin thickness times 3.7 $J \cdot cm^{-3} \cdot K^{-1}$ volumetric heat capacity equals 120 $\mu J \cdot cm^{-2} \cdot K^{-1}$). For the PIN system with the silicone support (largest thermal mass), where the thermal mass is 7.6 $mJ \cdot cm^{-2} \cdot K^{-1}$, the device thermal mass is equal to a skin thickness of 21 μm.

**Supplementary Note 6: Water vapor permeability**

In order to minimize the effect of the devices on skin hydration, the devices can be applied directly to skin with no supporting substrate, as discussed in the main text. In this case, the sensors are effectively a largely void mesh on the skin, leaving the majority of the skin in the region of the sensors open to air allowing for normal water

vapor transport from the skin. In the cases where a silicone support is used for robustness, the 50 μm thick silicone sheet has a small impact on skin hydration (Supplementary Fig. S8c) which results in a 5% (n = 6, range = 2.8% – 9.5%) change in skin hydration after 3 hours of continuous use on the forearm as measured by a commercially available impedance-based skin hydration sensor (Delfin MoistureMeterSC). This change in skin hydration appears to have minimal, if any, impact on long-term temperature measurements. Supplementary Figure S8b shows two sets of temperature readings from the IR camera throughout 70 min of mental stimulus experiment. One set is taken from a region through the sensor system, and the other is taken adjacent to the sensors (Supplementary Fig. S8a). During the first half of the experiment, the maximum difference in temperature reading is 0.3 °C, which could be the result of non-uniform temperature changes in the hand. It should also be noted that the readings taken through the sensor patch always result in a lower IR temperature reading, when they occur, and may be due to the lower emissivity of the sensor system causing a slight decrease in IR temperature reading. During the second half of the experiment, there is a larger difference in reading between regions, likely due to real non-unformities in the temperature change of the hand.

**Supplementary Note 7: Sensor response time**

As shown in Supplementary Figure S7a, a TCR element is embedded in a PI layer (of thickness $H_{PI}$) on top of a layer of solaris silicone elastomer (of thickness $H_{solaris}$). The TCR element in the experiment is very thin (e.g., ~50 nm) and has thermal conductivity and diffusivity (the ratio of thermal conductivity to volumetric heat capacity) much larger (> 1600 times) than the PI such that its effect on thermal analysis of the system can be neglected. The TCR element is at a distance $d$ below the top surface.

A warm ethylene glycol drop (or skin) on top of the PI layer heats up the entire system. The in-plane dimensions of the PI layer are much larger than its thickness such that the heat flux is mainly along the thickness direction, which can be represented by a one-dimensional heat transfer model

$$\frac{\partial T}{\partial t} - \alpha \frac{\partial^2 T}{\partial x^2} = 0 \qquad (1)$$

where $T$ is the temperature increase (from the ambient temperature), $\alpha$ is the thermal diffusivity, and the coordinate $x$ is along the thickness direction. The warm ethylene glycol (or skin) provides a constant temperature increase $T_0$ at the top,

$$T\big|_{x=0} = T_0 . \qquad (2)$$

The numerical analysis suggests that the natural convection at the bottom surface of solaris has a negligible effect and can be approximated by a thermal isolation condition[3]

DOI: 10.1038/NMAT3755

$$\left.\frac{\partial T}{\partial x}\right|_{x=H_{PI}+H_{solaris}} = 0 . \quad (3)$$

In addition, the temperature and heat flux, $-k\partial T/\partial x$, are continuous across the PI/solaris interface, where $k$ is the thermal conductivity. The initial condition is

$$T|_{t=0} = 0 . \quad (4)$$

The Laplace transform is used to solve Eqs. (1)-(4). The transformed temperature can be expanded into series. The temperature of the sensor, $T_{sensor}$, which is the same as the temperature of the PI at the same position $x=d$, can then be obtained by the inverse Laplace transform as

$$T_{sensor} = T_0 \sum_{n=0}^{\infty}\sum_{m=0}^{n}(-1)^m C_n^m \varphi^{n-m} \sum_{l=0}^{n-m} C_{n-m}^{l} \left\langle \begin{array}{l} erfc\left\{\left[(n-l+1)\nu+m+l+1-\mu/2\right]H_{PI}/\sqrt{\alpha_{PI}t}\right\} \\ -\varphi erfc\left\{\left[(n-l)\nu+m+l+1-\mu/2\right]H_{PI}/\sqrt{\alpha_{PI}t}\right\} \\ +erfc\left\{\left[(n-l)\nu+m+l+\mu/2\right]H_{PI}/\sqrt{\alpha_{PI}t}\right\} \\ -\varphi erfc\left\{\left[(n-l+1)\nu+m+l+\mu/2\right]H_{PI}/\sqrt{\alpha_{PI}t}\right\} \end{array} \right\rangle \quad (5)$$

where $C_n^m = \frac{n!}{m!(n-m)!}$, $\varphi = \frac{k_{solaris}/\sqrt{\alpha_{solaris}} - k_{PI}/\sqrt{\alpha_{PI}}}{k_{solaris}/\sqrt{\alpha_{solaris}} + k_{PI}/\sqrt{\alpha_{PI}}}$, $\nu = \frac{H_{solaris}}{H_{PI}}\sqrt{\frac{\alpha_{PI}}{\alpha_{solaris}}}$, $\mu = d/H_{PI}$, and *erfc* is the complementary error function[4].

The thermal properties of PI and solaris are $k_{PI} = 0.12$ W/(m·K), $\alpha_{PI} = 7.75*10^{-8}$m$^2$/s [5], $k_{solaris} = 0.186$ W/(m·K) and $\alpha_{solaris} = 1.08*10^{-7}$m$^2$/s [6] (from manufacturer), which give $\varphi = 0.135$. For such a small $\varphi$ and a much larger thickness of the solaris layer (e.g., $H_{solaris} = 60\mu$m) than the PI layer (e.g., $H_{PI} = 3.6$ or $6.0\mu$m) in experiments, Eq. (5) can be simplified to

$$T_{sensor} = T_0 \left\{ \begin{array}{l} erfc\left(\frac{\mu}{2}\frac{H}{\sqrt{\alpha_{PI}t}}\right) + erfc\left[\left(\nu+1-\frac{\mu}{2}\right)\frac{H}{\sqrt{\alpha_{PI}t}}\right] - erfc\left[\left(\nu+1+\frac{\mu}{2}\right)\frac{H}{\sqrt{\alpha_{PI}t}}\right] \\ +\varphi erfc\left[\left(1+\frac{\mu}{2}\right)\frac{H}{\sqrt{\alpha_{PI}t}}\right] - \varphi erfc\left[\left(1-\frac{\mu}{2}\right)\frac{H}{\sqrt{\alpha_{PI}t}}\right] \end{array} \right\} \quad (6)$$

The sensor response time is defined by the time at which the sensor temperature increase $T_{sensor}$ reaches 90% of $T_0$. For $H_{PI} - d = 1.2\mu$m and $H_{solaris} = 60\mu$m as in the experiment, the sensor response time is 3.7 ms for $H_{PI} = 3.6\mu$m and 13.1 ms for $H_{PI} = 6.0\mu$m. These agree reasonably well with the experimentally measured sensor response time (for $T_{sensor} = 0.9T_0$) of 4.2 ms and 12.2 ms for $H_{PI} = 3.6$ and $6.0\mu$m, respectively.

## Supplementary Note 8: Fourier analysis of temperature readings

Low frequency temperature oscillations were examined via Fourier transforms of temperature signals obtained by the TCR device, as well as the IR camera, on the ventral forearm. For the TCR device, the readings of each of the 16 elements in the TCR device were averaged to generate a one-dimensional time-domain signal. This signal was then resampled with a resampling factor of 3/100. This brought the original sample rate of 66.67 Hz (15 ms sample period) to 2 Hz to match the sample rate of the IR camera. The resampled data were then subjected to a digital elliptical filter with a cutoff frequency of 0.004 Hz. The outcome of this filtering operation had the filter startup transients removed, and was then subjected to FFT analysis. For the IR camera, the readings of each pixel in the ROI were averaged to generate a one-dimensional time-domain signal. The signal was then subjected to same elliptical filter and analysis as the TCR device signals. In order to verify that the prominent frequency peaks are physiologically generated and not measurement artifacts due to the electronics of the TCR device, control experiments were run under the same conditions as the epidermal oscillations test (see Methods), but with the TCR device placed on a black felt pad instead of human skin. The results, compared to the results from human skin, are shown in Supplementary Figure S8d and show that dominant peaks present on skin are absent on the felt pad.

## Supplementary Note 9: Mathematical modeling of reactive hyperemia

A two-dimensional heat transfer model was developed to determine the time-dependent temperature distribution in the tissues surrounding the artery during and after occlusion. A schematic illustration of the tissue geometry appears in Supplementary Figure S10, where a circular cross section is adopted for the wrist to simplify the analyses. The blood at body temperature flows through the circular artery embedded in the subcutaneous layer (mainly composed of fat), and heats the surrounding tissues. The heat exchange between the blood flow and the fat layer across the artery wall is modeled via a heat convection model[7], which linearly correlates the exchanged heat flux with the blood flow rate in the form of

$$q = \bar{h}_{artery-wall}\left(T_{body} - T_s\right) = \frac{\rho_b c_{pb} \omega_b(t)}{\pi D_{artery}}\left(T_{body} - T_s\right), \quad (7)$$

where $q$ is the heat flux flowing into the fat layer; $\rho_b$, $c_{pb}$, $\omega_b(t)$ are the density, specific heat capacity, and time-dependent flow of the blood; $D_{artery}$ is the diameter of the artery; $T_{body}$ and $T_s$ are the body temperature, and the temperature of fat at the artery wall, respectively; $\bar{h}_{artery-wall}$ is the equivalent heat transfer coefficient. Due to the heating from

DOI: 10.1038/NMAT3755

blood flow, the temperature redistributes in the surrounding tissues, which follows the temporal heat conduction equation of $\rho_j c_j \frac{\partial T_j}{\partial t} = k_j \left( \frac{\partial^2 T_j}{\partial x^2} + \frac{\partial^2 T_j}{\partial y^2} + \frac{\partial^2 T_j}{\partial z^2} \right)$ ($j$=1..4), where the subscript represents different tissues (with skin as $j$=1, fat as $j$=2, muscle as $j$=3, and bone as $j$=4). The free, outer surface of the skin has natural convection with air, which usually cools down the skin due to a lower room temperature than body temperature.

The solution of the heat transfer model includes two steps, which starts from the simulation of the steady-state heat conduction in the various tissues due to constant heating of blood flow, corresponding to the stage of pre-occlusion (Stage I). Then, by using the steady-state solution as an input, we further simulate the temporal variation of temperature in the tissues due to the application and release of occlusion, corresponding to the stage of vascular occlusion (Stage II) and reperfusion (Stage III), respectively. The blood perfusion keeps constant during Stage I, and varies with time during Stages II and III. Based on previous experimental data[6], the temporal variation of blood flow during these different stages can be well described by the following piecewise function[7,8]

$$\begin{aligned}
&\omega_b^{I}(t) = \omega_0,\ t \le t_{occ,st} \\
&\omega_b^{II}(t) = (\omega_0 - \omega_s)\exp(-t/\tau_0) + \omega_s,\ t_{occ,st} < t \le t_{occ,end} \\
&\omega_b^{III}(t) = \begin{cases} (\omega_{\max} - \omega_s)\sin^2\left[\pi(t - t_{occ,end})/(2t_{dw})\right] + \omega_s,\ t_{occ,end} < t \le (t_{occ,end} + t_{dw}) \\ (\omega_{\max} - \omega_f)\exp\left[-(t - t_{occ,end} - t_{dw})/\tau_h\right] + \omega_0,\ t > (t_{occ,end} + t_{dw}) \end{cases}
\end{aligned} \tag{8}$$

where $\omega_0$ represents the baseline blood flow and has the same value as that of the healthy tissue; $\omega_s$ is the blood perfusion after the occlusion is applied for a sufficiently long time, 60 s in the case of experiments here; $\omega_{max}$ is the maximum hyperemic blood flow; $\tau_0$ is a time constant depicting the falling speed of blood flow after occlusion is applied; $t_{dw}$ is the time required to reach the maximum hyperemic blood flow after the release of occlusion; $\tau_h$ indicates the rate at which the blood flow returns to the baseline value during the reperfusion; $t_{occ,st}$ and $t_{occ,end}$ denote the starting and ending times of the occlusion, respectively. Except for $t_{occ,st}$ and $t_{occ,end}$, which are known in experiments ($t_{occ,st}$=300 s, $t_{occ,end}$=360 s), there are six parameters in this model of reactive hyperemia which can be varied to simulate the temperature history of blood perfusion. The aim of the thermal analyses is to obtain an optimized set of parameters that can best match the experiment data of temperature-time profile at the skin surface right above the artery. Note that the baseline blood flow $\omega_0$ does not involve the occlusion process, and thus it can be determined using the temperature value measured before the occlusion (Stage I). The blood flow $\omega_s$ and time parameter $\tau_0$ (only related to Stage II) are determined by the measured temperature-time profile during Stage II, and the other three parameters ($\omega_{max}$, $t_{dw}$ and $\tau_h$,) are determined by the experimental data

during Stage III. Besides the baseline flow rate ($\omega_0$), there are five parameters in our simulations, i.e., $\alpha=\omega_s/\omega_0$, $\beta=\omega_{max}/\omega_0$, $\tau_0$, $t_{dw}$ and $\tau_h$, whose ranges are listed in Supplementary Table 1, based on reported experiments[7,8].

Finite element analyses (FEA) were carried out to solve the transient heat transfer equation, and determine the temperature distribution numerically. 4-node linear heat transfer elements were used, and refined meshes were adopted to ensure the accuracy. The boundary conditions include the heat convection at the artery wall with blood flow of body temperature (the effective heat transfer coefficient was given by Eq. (7)), and the natural convection at the outer surface of skin with air of room temperature. The geometric and thermal-physical properties of various tissues are given in Supplementary Table 2. For the reactive hyperemia model described above, the parameters of blood flow are determined by numerical calculations as $\omega_0$=15 mL/min (9.8 cm/s using a vessel diameter of 1.8 mm), $\omega_s$=3 mL/min, $\omega_{max}$=150 mL/min (98 cm/s), $\tau_0$=5 s, $t_{dw}$=15 s, $\tau_h$=45 s. For this set of parameters, the temperature-time profile obtained from FEA agrees reasonably well with the experiment results (Fig. 4d). The temperature distributions in the tissues are demonstrated in Supplementary Figure S11 for four typical stages before and after the occlusion, which clearly shows that the heating effect localizes nearby the artery and decreases rapidly away from the artery.

## Supplementary Note 10: Transient plane source analysis

Thermal conductivities of skin are determined using the transient plane source (TPS) analysis[9,10] in an iterative, empirical fashion. The plane sources in this case are the individual square elements of the TCR device. The experiment consists of a 6 second measurement procedure as described in the Methods, with 2 s of heating at with 1.5 mA applied current, which generates 2 mW of power in the 1 mm x 1 mm square element. The temperature rise in the TCR element during heating is measured in the same fashion as in all experiments presented here, by measuring the voltage drop with a known applied current. The transient heating of a square plane has been shown to follow

$$\overline{\Delta T}(\tau) = \frac{P_0}{4a\pi^{1/2}k} H(\tau) \tag{9}$$

Where $P_0$ is the power output from the TCR element and approximated as constant during heating due to the <2% resistance change during heating, $2a$ is the width of the heater square ($a$ = 0.5 mm in this case), $k$ is the thermal conductivity, $\Delta T$ is the average temperature rise in the heater, $\tau$ is given by

$$\tau = \left(\frac{\alpha t}{a^2}\right)^{1/2} \tag{10}$$

DOI: 10.1038/NMAT3755

where $\alpha$ is the thermal diffusivity of the medium, and $H(\tau)$ is given by

$$H(\tau) = \int_0^{\tau} dv \left\{ \mathrm{erf}(v^{-1}) - \pi^{-1/2} v[1 - \exp(-v^{-2})] \right\} \quad (11)$$

where $\tau$ is solved iteratively to generate a linear relation of $\Delta T(\tau)$ with $H(\tau)$, where $H(\tau)$ is solved numerically. Thermal conductivity, $k$, is then determined from this relation.

In our studies, deionized water is used as a calibration medium of known thermal conductivity (0.6 $W \cdot m^{-1} \cdot K^{-1}$) to generate an effective length value for $a$, which is then used in all subsequent measurements to determine thermal conductivity. The determination of an effective length allows us to correct for geometrical differences from an ideal plane source, such as our serpentine wire structure and finite plane, as well as the presence of the silicone backing followed by air on the back of the sensor. It is also noted that the probing depth of the measurement is given as

$$\Delta_p = \beta(\alpha t_{max})^{1/2} \quad (12)$$

where $\beta$ is a constant of approximately 1 and $t_{max}$ is the time length of heating, which gives a probing depth of approximately 500 μm for our experiments here.

## References


1 Sondheimer, E. H. The Mean Free Path of Electrons in Metals. *Adv Phys* **1**, 1-42 (1952).

2 Cohen, M. L. Measurement of Thermal-Properties of Human-Skin - Review. *J Invest Dermatol* **69**, 333-338 (1977).

3 Lu, C. F. *et al.* A thermal analysis of the operation of microscale, inorganic light-emitting diodes. *P Roy Soc a-Math Phy* **468**, 3215-3223 (2012).

4 Andrews, L. *Special Functions of Mathematics for Engineers (second edition)*. (SPIE Press, 1997).

5 Technical datasheet from manufacturer, Dupont Co.

6 Technical datasheet from manufacturer, PSC A/S.

7 Deshpande, C. *Thermal analysis of vascular reactivity* MS thesis, Texas A&M University, (2007).

8 Akhtar, M. W., Kleis, S. J., Metcalfe, R. W. & Naghavi, M. Sensitivity of digital thermal monitoring parameters to reactive hyperemia. *Journal of Biomechanical Engineering* **132** (2010).

9 Gustafsson, S. E. Transient plane source techniques for thermal conductivity and thermal diffusivity measurements of solid materials. *Review of Scientific Instruments* **62**, 797-804 (1991).

10 Rosenbaum, E. J. *Thermal properties and characterization of methane hydrates* M.S. thesis, University of Pittsburgh, (2001).

11 Fiala, D., Lomas, K. J. & Stohrer, M. A computer model of human thermoregulation for a wide range of environmental conditions: The passive system. *Journal of Applied Physiology* **87**, 1957-1972 (1999).

12 Song, W. J., Weinbaum, S., Jiji, L. M. & Lemons, D. A combined macro and microvascular model for whole limb heat transfer. *Journal of Biomechanical Engineering* **110**, 259-268 (1988).

13 Sieg, P., Hakim, S. G., Bierwolf, S. & Hermes, D. Subcutaneous fat layer in different donor regions used for harvesting microvascular soft tissue flaps in slender and adipose patients. *International Journal of Oral and Maxillofacial Surgery* **32**, 544-547 (2003).

14 Shen, H. *et al.* A genomewide scan for quantitative trait loci underlying areal bone size variation in 451 Caucasian families. *Journal of Medical Genetics* **43**, 873-880 (2006).

15 Shima, H., Ohno, K., Michi, K. I., Egawa, K. & Takiguchi, R. An anatomical study on the forearm vascular system. *Journal of Cranio-Maxillo-Facial Surgery* **24**, 293-299 (1996).

16 McCartney, C. J. L., Xu, D., Constantinescu, C., Abbas, S. & Chan, V. W. S. Ultrasound Examination of Peripheral Nerves in the Forearm. *Regional Anesthesia and Pain Medicine* **32**, 434-439 (2007).

17 Kathirgamanathan, A., French, J., Foxall, G. L., Hardman, J. G. & Bedforth, N. M. Delineation of distal ulnar nerve anatomy using ultrasound in volunteers to identify an optimum approach for neural blockade. *European Journal of Anaesthesiology* **26**, 43-46 (2009).

DOI: 10.1038/NMAT3755

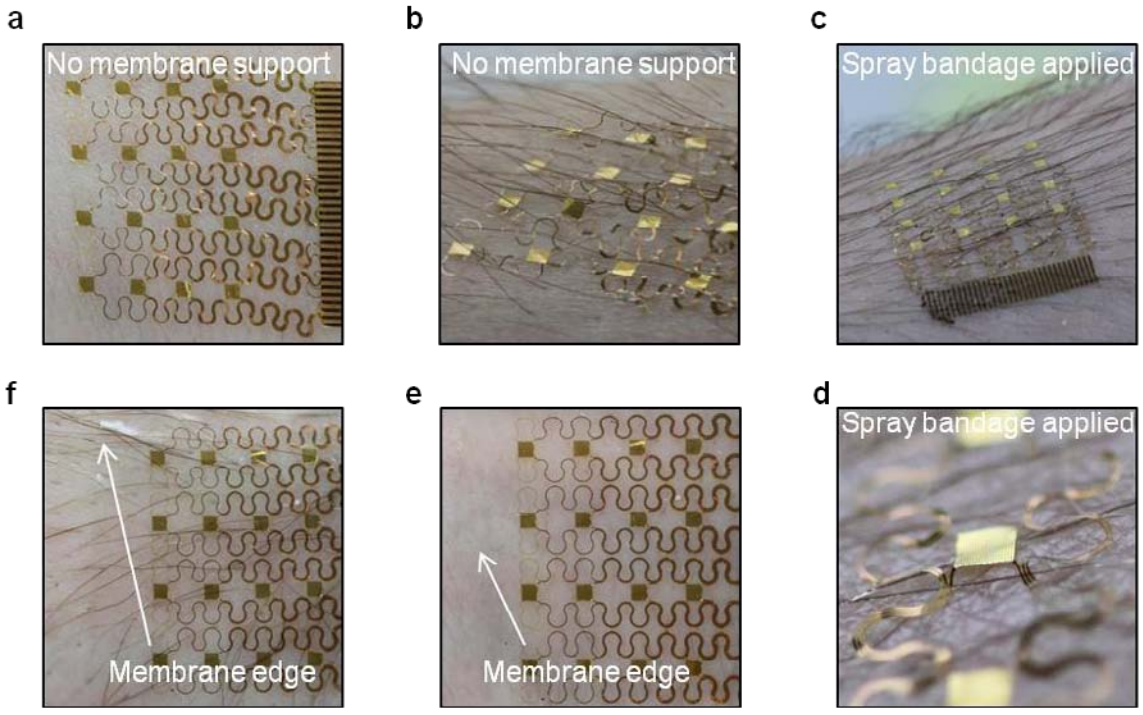


**Supplementary Figure S1: Effects of hair on adhesion.** (**a**) A 4x4 TCR array with no supporting membrane applied to an area of hairless skin. (**b**) An array with no supporting membrane applied to an area with significant hair. Some hair can rise between individual elements in the array, but adhesion is significantly frustrated. (**c**) An array with no supporting membrane applied to an area with significant hair following the application of commercial spray-on bandage. Adhesion is significantly improved; however hair directly beneath a sensor element may limit intimate thermal contact (**d**). (**e**) An array with a supporting silicone membrane applied to an area of hairless skin. (**f**) An array with a supporting silicone membrane applied to an area with significant hair. Here, the supporting membrane helps to flatten the hair, to allow for device adhesion.

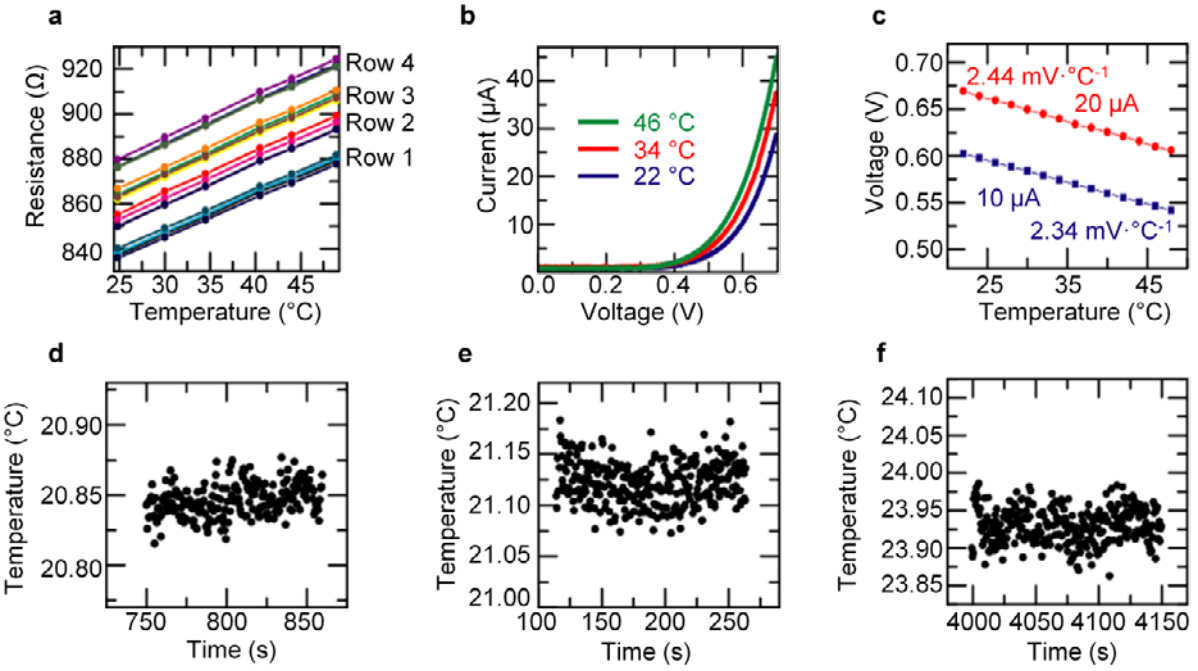


**Supplementary Figure S2: Sensor calibration and noise measurements.** (**a**) 4 x 4 TCR sensor array temperature calibration. Calibration curves appear in four groups of four sensors each, due the differing interconnect distances leading to each row of sensors. (**b**) Representative I-V curves of a single sensing element from a PIN device, at different temperatures. (**c**) Representative temperature calibration from single element of a PIN device at 10 μA (blue) and 20 μA (red). (**d**) Representative TCR device measurement at 2 Hz in air (std. dev = 0.012 °C) and (**e**) on skin (std. dev. = 0.021 °C). (**f**) Representative IR measurement at 2 Hz of skin (std. dev. = 0.024 °C, trend is removed).

DOI: 10.1038/NMAT3755

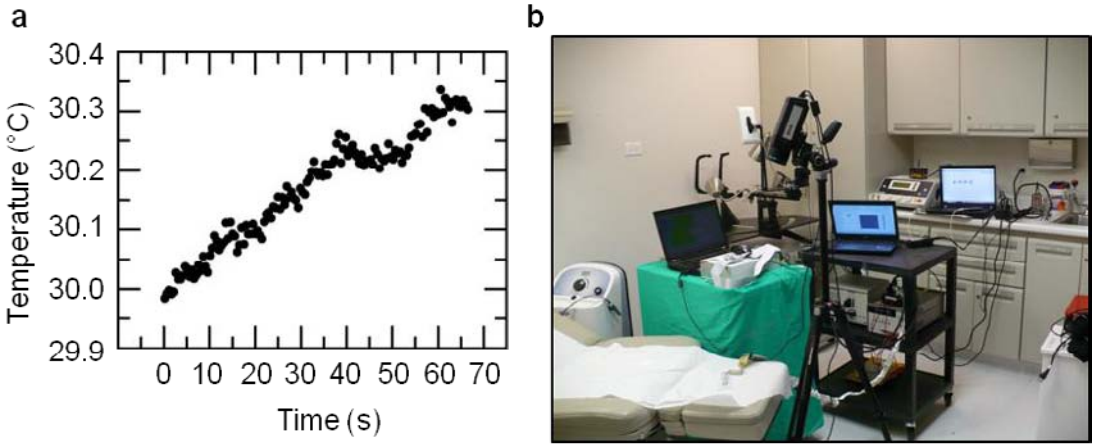


**Supplementary Figure S3: Noise measurements in clinical exam room.** (**a**) Temperature measurements on skin from a TCR array element taken in a clinical exam room at Northwestern Memorial Hospital in Chicago, IL (std. dev. = 0.023 °C, after linear trend is removed). Measurements were performed while simultaneously running many pieces of electrical equipment, beyond what is expected in a typical exam room, as shown in (**b**).

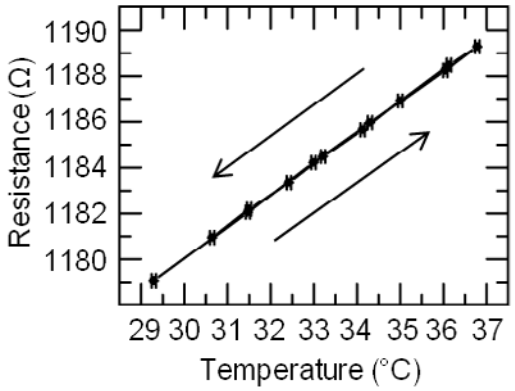


**Supplementary Figure S4: Representative hysteresis of TCR array element.** Resistance of a TCR array element as measured during a heating and cooling cycle on a hotplate (~0.5 °C/min heating, ~0.2 °C/min cooling). Temperature is determined using an IR camera. Data shows no hysteresis within the uncertainty of the measurement (<73 mK. IR camera sensitivity of 50 mK, as stated by manufacturer. TCR device sensitivity of 23 mK, as stated in main text). All measurements fall within 73 mK of a linear fit line, with points randomly scattered above and below the fit during both heating and cooling.

DOI: 10.1038/NMAT3755

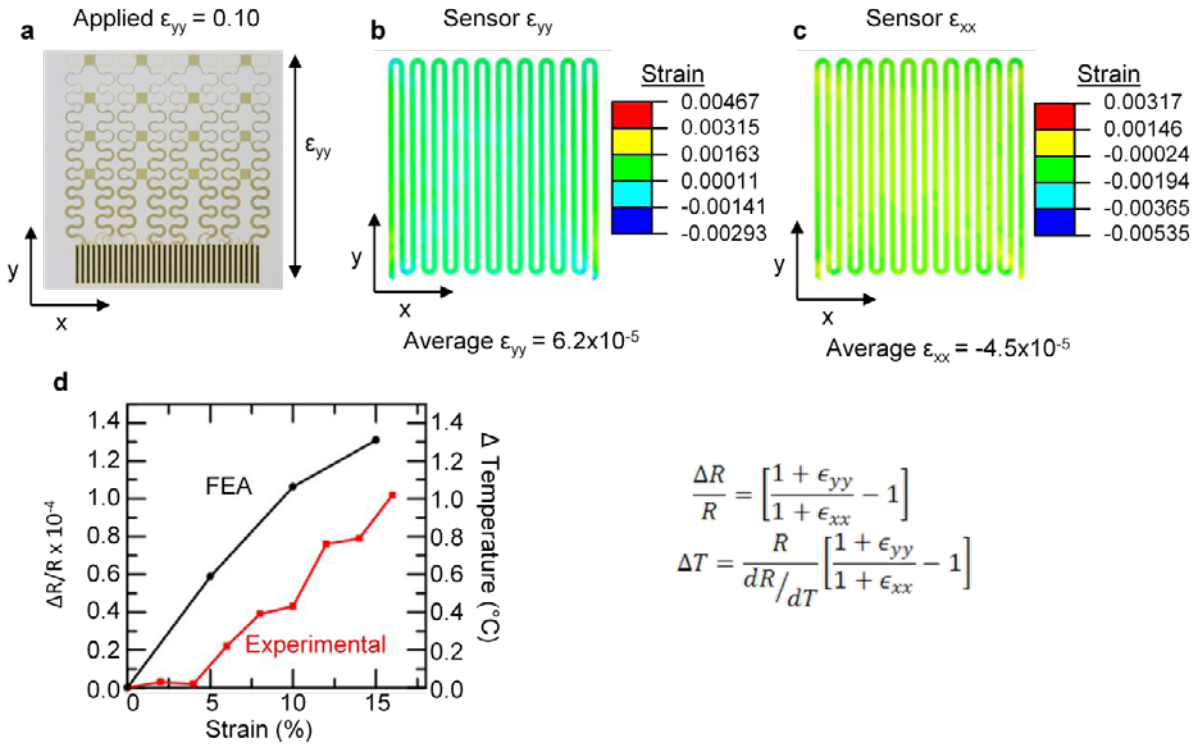


$$\frac{\Delta R}{R} = \left[\frac{1+\epsilon_{yy}}{1+\epsilon_{xx}} - 1\right]$$

$$\Delta T = \frac{R}{dR/dT}\left[\frac{1+\epsilon_{yy}}{1+\epsilon_{xx}} - 1\right]$$

**Supplementary Figure S5: Strain in TCR sensors.** (**a**) Optical image of 4 x 4 TCR sensor array showing representative direction of applied strain. (**b**) FEA results of 10% applied strain in y-direction to substrate showing the resultant $\varepsilon_{yy}$ strain distribution of a TCR sensor and (**c**) $\varepsilon_{xx}$ strain distribution of a TCR sensor. (**d**) FEA (black) and experimental (red) results of applying strain to substrate in the y-direction, showing resistance change due to strain and resultant error in temperature reading.

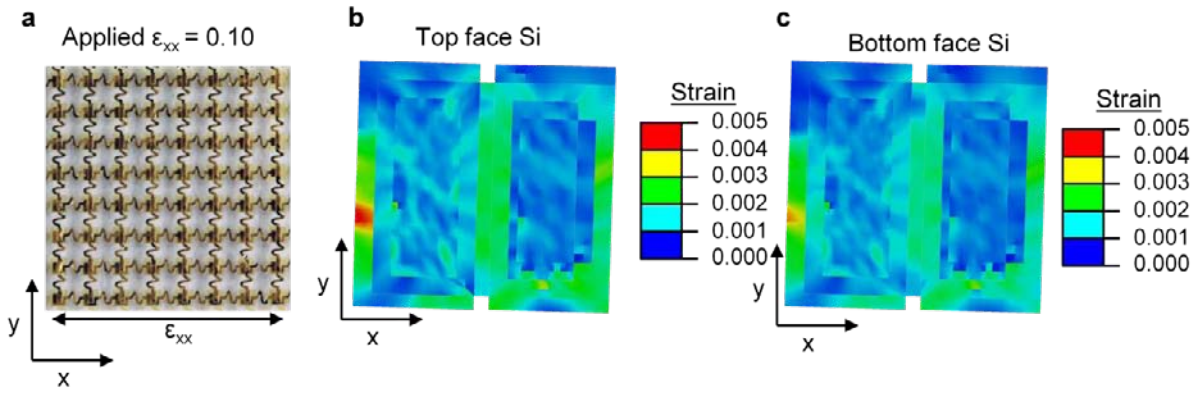


**Supplementary Figure S6: Strain in PIN sensors.** (**a**) Optical image of 8 x 8 PIN sensor array showing representative direction of applied strain. (**b**) FEA results of 10% applied strain in x-direction to substrate showing the resultant top surface Si strain distribution of a PIN sensor and (**c**) bottom surface Si strain distribution of a PIN sensor.

DOI: 10.1038/NMAT3755

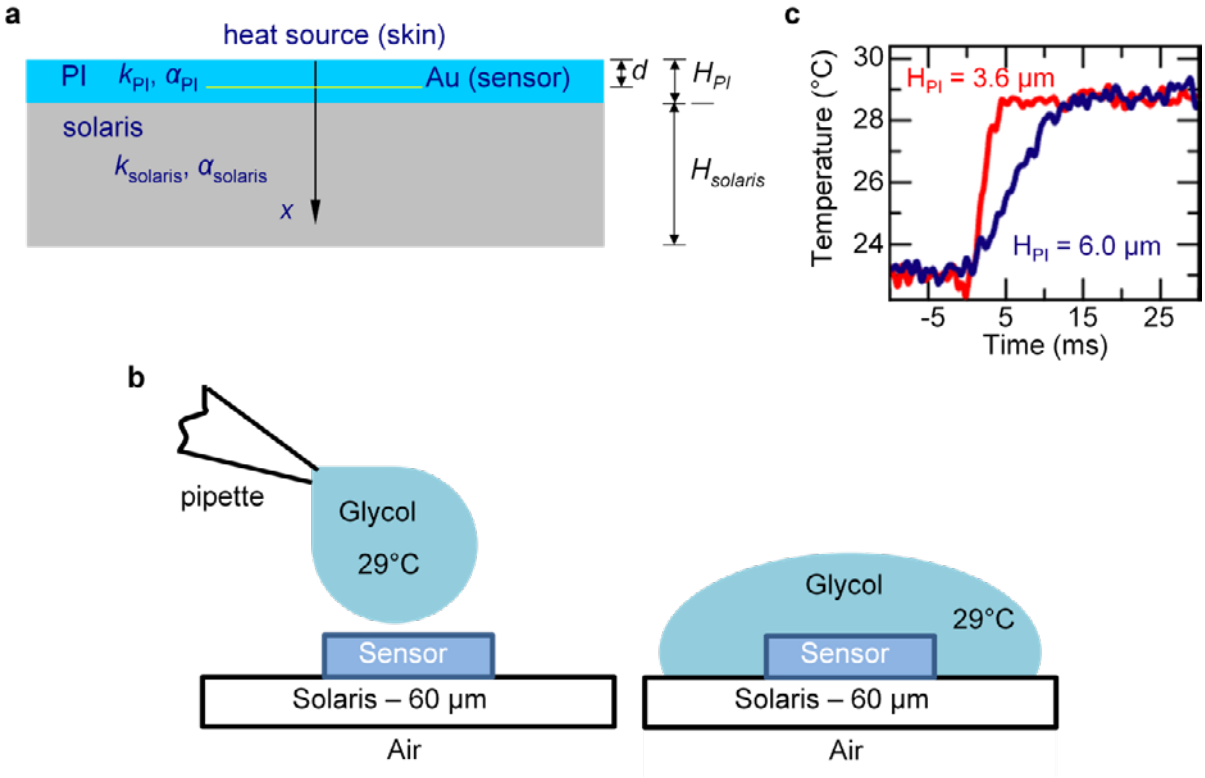


**Supplementary Figure S7: Sensor response time.** (**a**) Layers used in analytical modeling to determine sensor response time on skin. (**b**) Experimental setup for measuring sensor response time. A warm drop of ethylene glycol, which has similar thermal properties to skin, is dropped onto the sensor. (**c**) Experimental sensor response time to warm glycol droplet. The time required for the sensor to reach 90% of the total temperature change is 3.7 ms and 13.1 ms for the case of $H_{PI}$ = 3.6 µm and $H_{PI}$ = 6.0 µm, respectively.

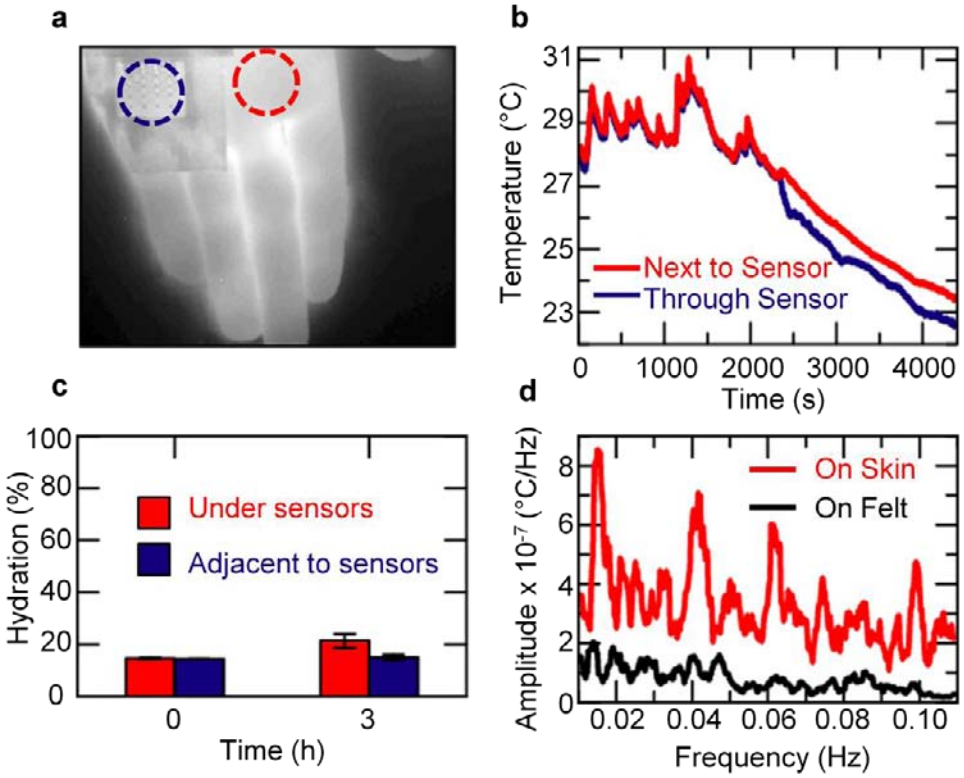


**Supplementary Figure S8: Effects on physiology.** (**a**) IR image showing locations used for comparison temperature data. (**b**) Comparison of IR temperature data through the TCR device (red) and next to the TCR device (blue) obtained during a mental stimulus experiment. (**c**) Skin hydration changes after wearing TCR device for 3 hours as measured by commercial Delfin Moisture Meter. (**d**) Comparison of frequency power spectrum measured by TCR device during 1 hour on skin (red) and a felt pad (black).

DOI: 10.1038/NMAT3755

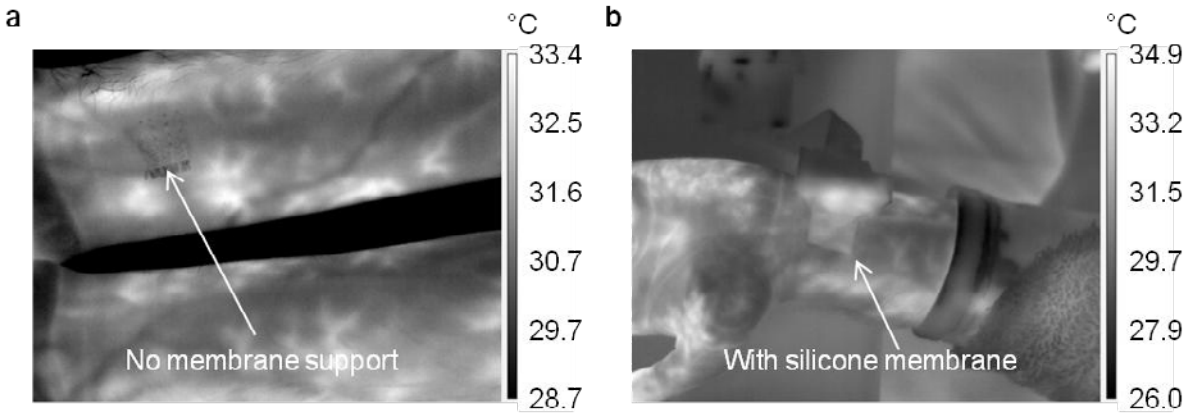


**Supplementary Figure S9: Effect on skin temperature during profuse sweating.** IR images of forearm during profuse sweating immediately following high-intensity aerobic exercise while wearing (**a**) a device with no supporting silicone membrane, and (**b**) a device with a thin silicone membrane substrate. The device with no silicone membrane (**a**) does not appear to have any effect on local skin temperature, while the device with a silicone membrane (**b**) causes a ~2 °C rise in temperature directly beneath the membrane, as compared to adjacent skin.

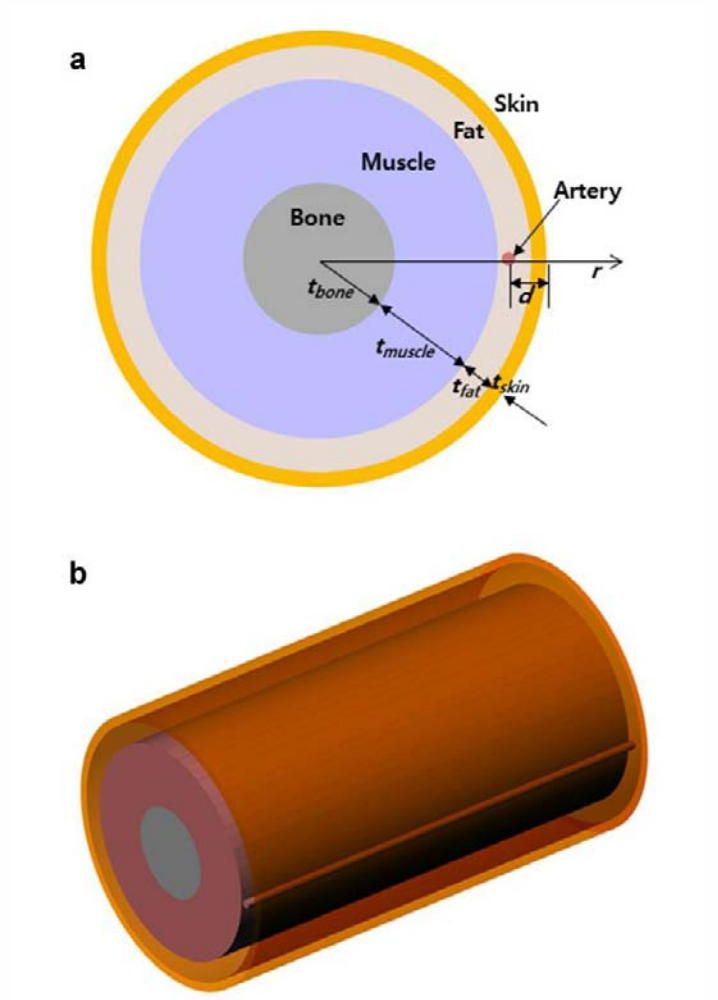


**Supplementary Figure S10: Schematic illustration of the wrist model for simulations:** (**a**) the cross-sectional view. (**b**) three-dimensional view.

DOI: 10.1038/NMAT3755

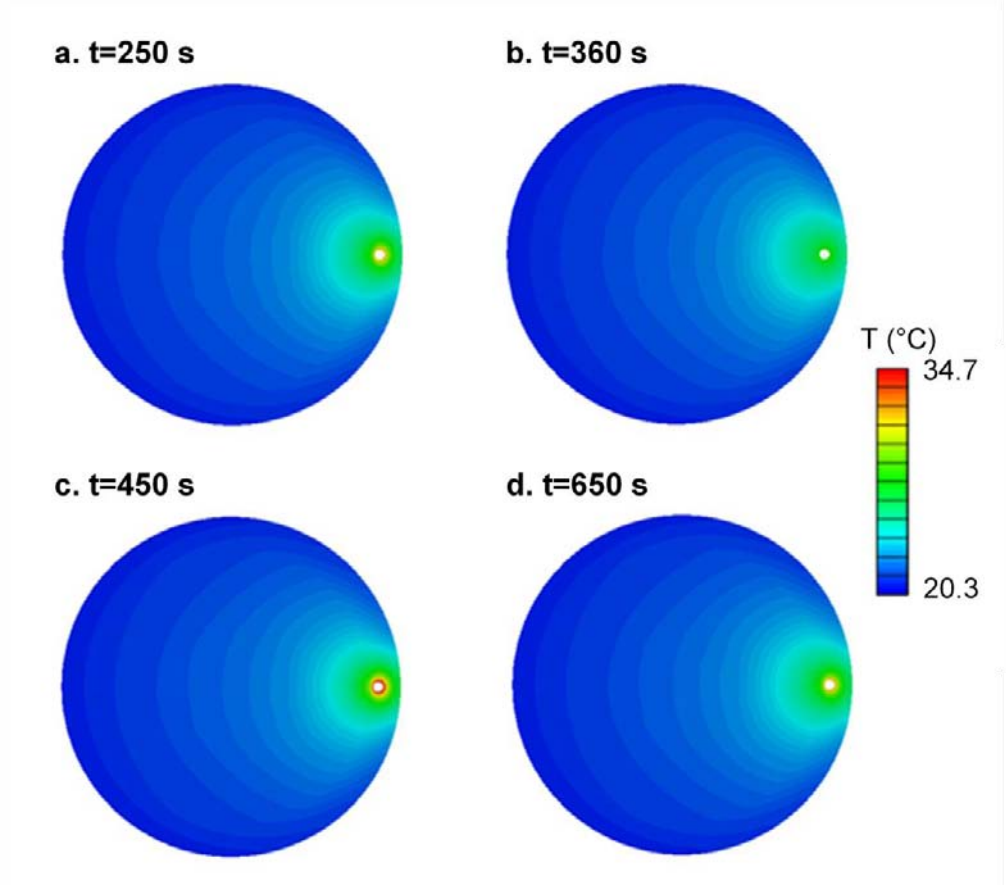


**Supplementary Figure S11: FEA results on the temperature distribution in the tissues of blood flow model at four typical stages: (a)** t=250 s, before occlusion. **(b)** t=360 s, at the release of occlusion. **(c)** t=450 s, when the temperature of skin surface is close to its maximum value. **(d)** t=650 s, when the temperature nearly returns to the baseline level after the occlusion.

**Supplementary Table 1. The parameter range in the model of reactive hyperemia for simulations.**

| | $\alpha=\omega_s/\omega_0$ | $\beta=\omega_{max}/\omega_0$ | $\tau_0$(s) | $t_{dw}$ (s) | $\tau_h$(s) |
|---|---|---|---|---|---|
| Range | [0, 0.20] | [2, 10] | [1, 5] | [15, 45] | [45, 80] |

**Supplementary Table 2. The geometric and thermal-physical properties of various tissues for the wrist, where *t* denotes the thickness, *D* is the diameter of the artery, and *d* is the depth of the artery.**

| Parameter | Skin | Fat | Muscle | Bone | Blood |
|---|---|---|---|---|---|
| $\rho$ (kg/m$^3$)[7,11] | 1085 | 850 | 1085 | 1357 | 1069 |
| $c_p$ (J/kg/K)[7,11] | 3680 | 2300 | 3768 | 1700 | 3659 |
| $k$ (W/m/K)[7,11] | 0.47 | 0.16 | 0.42 | 0.75 | / |
| $t$ (mm)[12-14] | 1.0 | 4.4 | 13.6 | 10.0 | / |
| $D$ (mm)[15] | / | / | / | / | 1.8 |
| $d$ (mm)[16,17] | / | / | / | / | 4.0 |